The diagenetic history of the giant Lacq gas field, witness to the apto-albian rifting and the Pyrenean orogeny, revealed by fluid and basin modeling

Alexy Elias Bahnan, Jacques Pironon, Cédric Carpentier, Guillaume Barré, Eric Gaucher

The diagenetic history of the giant Lacq gas field, witness to the Apto-Albian rifting and the Pyrenean orogeny, revealed by fluid and basin modeling

Alexy Elias Bahnan[a*], Jacques Pironon[a], Cédric Carpentier[a], Guillaume Barré[b,c], Eric C. Gaucher[b]

[a] Université de Lorraine, CNRS, CREGU, GeoRessources, F-54000 Nancy, France

[b] TOTAL, CSTJF, F-64018 Pau Cedex, France

[c] Université de Pau et des Pays de l'Adour, CNRS, TOTAL, LFCR, F-64000 Pau, France

[*] alexy.elias-bahnan@univ-lorraine.fr

Highlights

- Combining several equations of state allows the P-T modeling of H_2S-bearing fluids.
- The rifting and the orogenic stages influenced the diagenesis of the Deep Lacq reservoir.
- Hydrocarbon maturation, dolomitization and calcite precipitation were controlled by the rifting event.
- The reservoir was infilled with gas during the Pyrenean orogeny
- TSR did not occur *in-situ.*

Abstract

The link between fluid circulation schemes and basin histories remain one of the most valuable tools to understand the diagenetic evolution of petroleum reservoir. This study proposes a diagenetic model for the Deep Lacq reservoir constrained by petrography, geochemistry, fluid inclusions studies and basin modeling analyses. Drill cores penetrating the 3000 meters deep Late Jurassic to Early Cretaceous “Deep Lacq” reservoirs, in the Aquitaine basin SW France, were used to investigate how the geodynamic evolution of the basin influenced the diagenesis of petroleum reservoirs. This basin experienced a phase of rifting during the Lower Cretaceous followed by inversion and compression during the Paleogene. Petrographic and geochemical results indicate that early diagenesis involved bacterial activity and early dolomitization. Fluid thermodynamic modeling, coupled with the reconstruction of the basin history provided insight into the timing of diagenetic fluid circulations. Burial diagenesis involved a rift-related dolomitization episode linked mainly to the recrystallization of earlier dolomites and the circulation of deep hot fluids connected to the Triassic evaporites. The dolomitizing fluids circulated at temperatures close to 136-144°C and pressures of 338-386 bars, during the Aptian (120-116Ma). During the post-rift uplift and its subsequent thermal re-equilibration, multiple fluid pulses precipitated coarse blocky calcites. These Ca-rich fluids circulated between 109 and 97 Ma, at high-pressure conditions at around of 704-766 bars and with temperatures of 146-156°C. The circulation of another fluid pulse that resulted in the precipitation of anhydrite cements is linked to the onset of the Pyrenean orogeny. No evidence that support *in-situ* TSR reactions were found, which suggest migration of TSR-related H_2S from a kitchen in the deeper parts of the basin. This multi-modeling approach show how the detailed

thermodynamic analyses of fluid inclusions can add valuable constraints on a diagenetic model and eventually link it to the larger-scale basin's history.

Keywords: Lacq petroleum system, Aquitaine basin, fluid inclusion modeling, basin modeling, sulfur-rich fluid system, TSR.

1 Introduction

The circulation of diagenetic fluids in petroleum reservoirs can be strongly influenced by the geologic history of the basin (Beaudoin et al., 2014, 2015; Salardon et al., 2017; Renard et al., 2019; Elias Bahnan et al., 2020). In the Aquitaine foreland basin, north of the Pyrenees Mountains (SW France), several hydrocarbon fields are located in Jurassic and Cretaceous reservoirs (Biteau et al., 2006). The giant Lacq field is part of the Lacq petroleum system with productive reservoirs extending over 320 km^2, a gas column reaching 3100 m and reserves in the order of 8.9 trillion cubic feet (Biteau et al., 2006). The exploitation of this gas field was a pioneering achievement at the time of its discovery in 1951. The high pressure (675 bar) and temperature (135°C) with a dangerous gas composition (15,2% H_2S, 9,7% CO_2; 69,2% C_1, 5,3% C_{2+}) (Le-vot et al., 1996) made it necessary to build an innovative desulfurization plant in 1957, still operational till present day.

The anticlinal structure of Deep Lacq is the result of the superposition of Jurassic rifting and Early Cretaceous rifting events, later inverted during the Late Cretaceous and the Paleogene (Sibuet et al., 2004; Jammes et al., 2010, 2009; Clerc and Lagabrielle, 2014; Mouthereau et al., 2014; Corre et al., 2016; Teixell et al., 2016; Vacherat et al., 2016). These events had significant control on the types, sources, chemistries and circulation mechanisms of the diagenetic fluids in the Aquitaine basin, as previously documented in the Rousse field (Renard et al., 2019), in the Upper Lacq oil reservoir (Elias Bahnan et al., 2020) and in the Chaînons Béarnais (Incerpi et al., 2020; Motte et al., 2021; Salardon et al., 2017). However, despite its importance as the most strategic reservoir in France during the 1970s (Biteau et al., 2006), no models were yet proposed to explain the diagenesis of Deep Lacq.

This study focuses on the Kimmeridigian-Barremian Deep Lacq gas field and aims to present a diagenetic model describing the different types, sources and circulation schemes of diagenetic fluids at different phases of the complex geological history that the Aquitaine basin has

experienced. The diagenetic events described in this research are placed in a geodynamic perspective that allows a better understanding of fluid activity during a complete Wilson cycle. Starting from a tectonic quiescence state and proceeding to early rifting, hyperextension, post-rift subsidence and ending with orogenesis, fluid-rock interactions are examined at each step. The case study presented in this work can be used as an example to compare diagenetic models of petroleum reservoirs in basins that experienced a similar geodynamic history as the Aquitaine. Examples include the Dengying reservoirs of the SW Sichuan basin (Wu et al., 2016), the Jurassic carbonates of Mount Lebanon (Nader, 2003), the Mobile Bay Jurassic Norphlet Formation of the Gulf of Mexico (Mankiewicz et al., 2009), the Níspero deeply buried Lower Cretaceous carbonate reservoir in the Gulf of Mexico (Bourdet et al., 2010), the Devonian Southesk-Cairn carbonate complex in Alberta, Canada (Machel and Buschkuehle, 2008), etc… The significance of this work is the use of multi-scale modeling approaches to extrapolate µm-scale fluid inclusions to basin-scale geodynamic events of the Aquitaine basin.

2 Geology and stratigraphy

The Deep Lacq reservoir is part of the Lacq petroleum system in the Arzacq sub-basin, south of the Aquitaine basin (Fig. 1). The Upper Lacq reservoir (Elias Bahnan et al., 2020) is separated from Deep Lacq by the Sainte Suzanne Marls. Since the target of this work is Deep Lacq, only the Jurassic to Early Cretaceous formations will be discussed. The genesis of the Aquitaine basin and the complete stratigraphic column of Lacq have been extensively described and detailed in a previous work (Elias Bahnan et al., 2020).

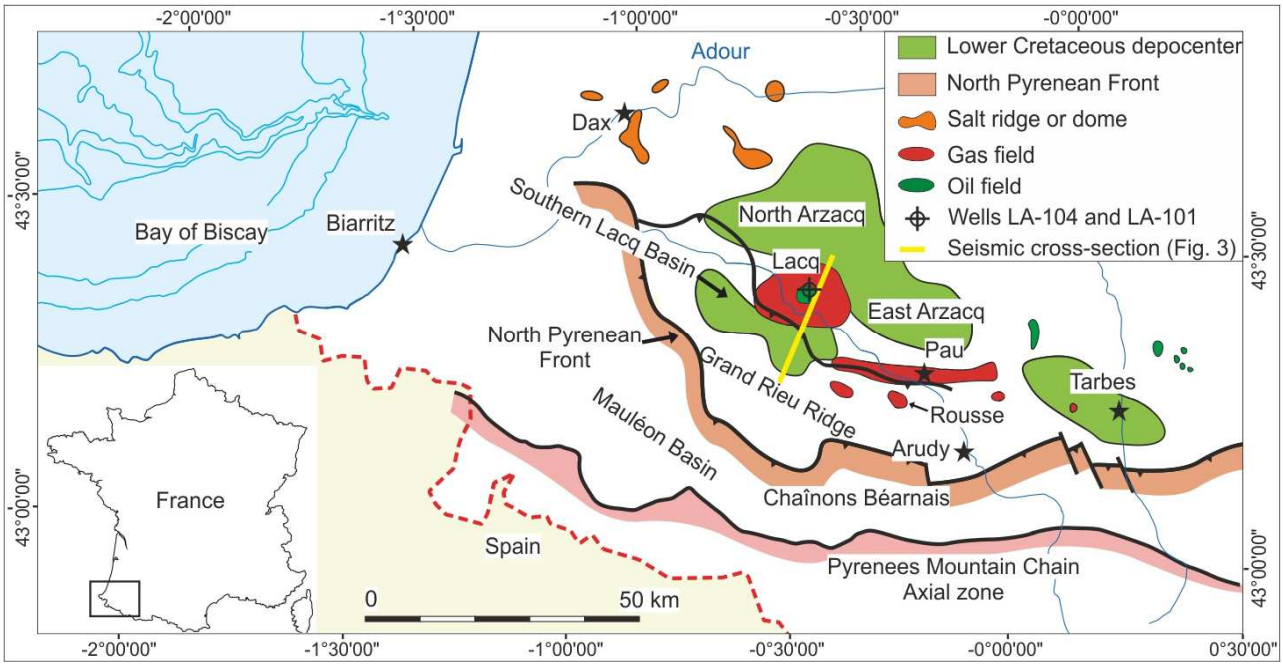

Figure 1. Structural map of the SW Aquitaine basin, showing the main structural elements, Cretaceous rift basins and hydrocarbon fields (modified after Biteau et al., 2006 and Elias Bahnan et al., 2020).

A simplified lithostratigraphic column with the main geodynamic events is compiled in figure 2. The basal fluvial sandstones (Red sandstone), limestones and dolomites (Muschelkalk) and evaporites (Keuper) constitute the Triassic formations (Fig. 2) (Lucas, 1985; Fréchengues et al., 1990; Le Marrec et al., 1995). The Carcans Dolomites is the first Jurassic formation followed by the Liassic anhydride unit (Curnelle and Dubois, 1986). The Mézos formation is a clay-rich peloidal limestone that was deposited during the mid-Jurassic (Le-Marrec et al., 1995). The Kimmeridgian is represented by the Cagnotte and Lons formations. The latter is composed of organic-rich marly limestones and dolomites and constitutes an important source rock for the Lacq petroleum system (Connan and Lacrampe-Couloume, 1993). The Late Jurassic Mano dolomite formation, an important reservoir in the Deep Lacq petroleum system, overlies the major source rock of the Lons formation (Fig. 2).

The Barremian deposits are subdivided into four formations, from bottom to top (Fig. 2): Algal Limestones, Lower Annelids Limestones, Laterlog shales, and Upper Annelids Limestone Formations (Le Marrec et al., 1995). All formations between the Mézos and the Upper Annelids (inclusive) constitute the main reservoirs of Deep Lacq (Biteau et al., 2006). Rift-related subsidence during the hyperextension created enough accommodation space for the deposition of nearly 600m of silty marls of the Sainte-Suzanne formation, which serve as an important seal for the Deep Lacq reservoirs (Biteau et al., 2006).

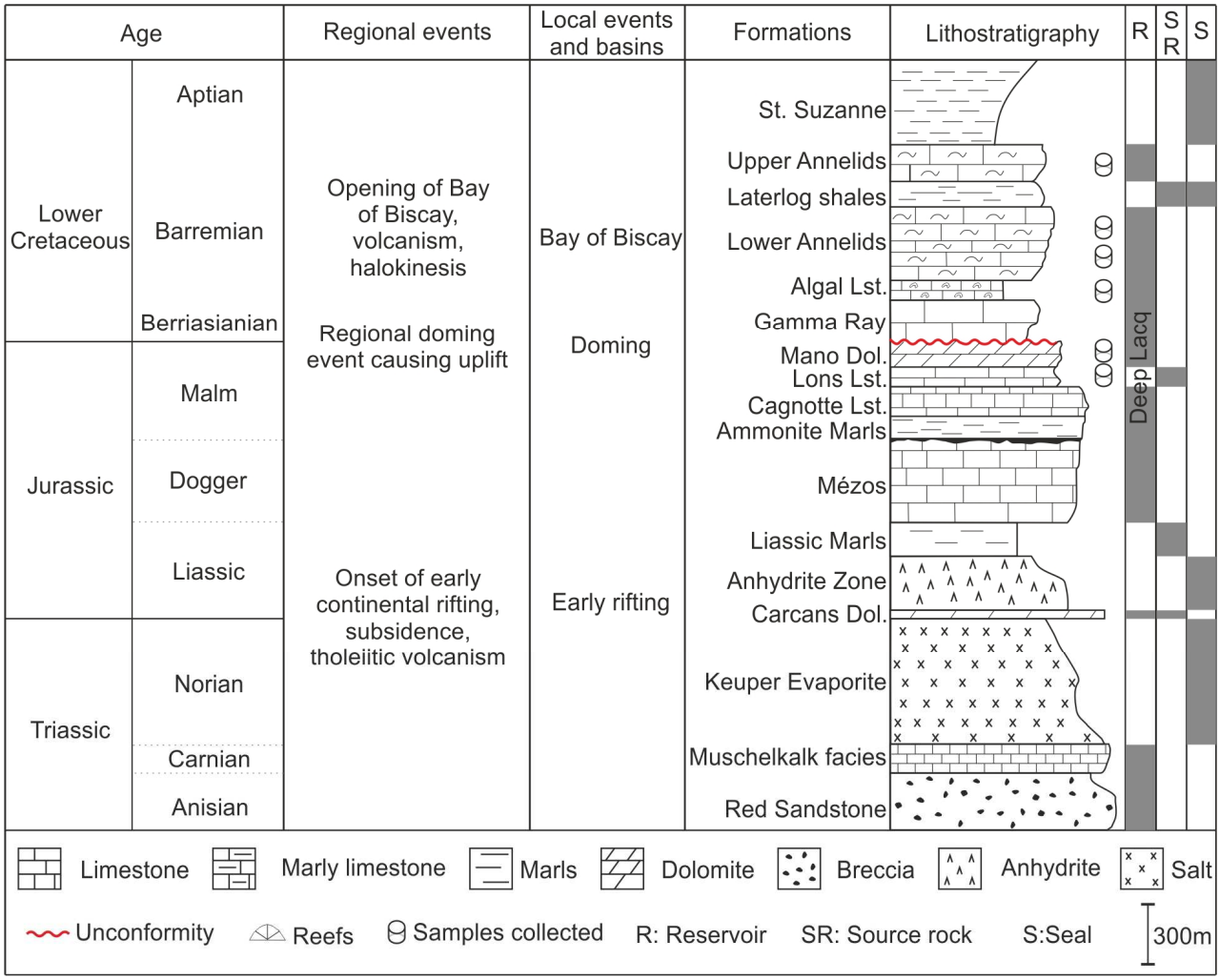

Figure 2. Simplified stratigraphic column of the Deep Lacq reservoir, source rocks and seals. The summary of the main tectonic events is also added. (Modified from Elias Bahnan et al., 2020).

3 Material and methods

3.1 Sampling

The studied core samples of Deep Lacq were obtained from wells LA-101 (Latitude: 43.420648°; longitude: -0.619980°) and LA-104 (Latitude: 43.420421°; longitude: -0.638811°) (Figs. 1 and 3). Additional public data on these wells can be found at the French national geological survey website (BRGM: infoterre.brgm.fr). Following the same strategy as that described by Elias Bahnan et al. (2020) for Upper Lacq, these wells were selected after a preliminary evaluation of nearly 600 thin sections provided from the archives of TOTAL. Targeted formations include the Lons, Mano, Algal and Annelids formations (Fig. 2) and the selected samples contain abundant coarse cement phases, fractures, veins, stylolites and cross-cutting relationships observable at the macroscopic scale.

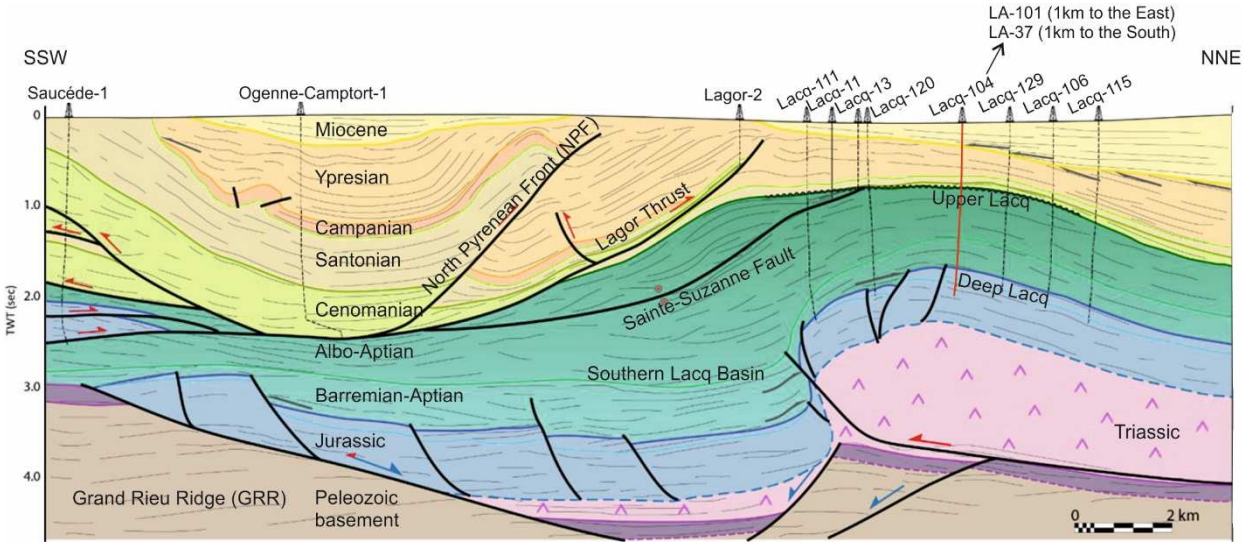

Figure 3. Interpreted seismic line passing NNE-SSW across the Lacq structure in the Arzaq basin (See Fig. 1 for location). No depth-velocity model was available to convert the TWT scale to meters. Instead, drilling reports indicate that well LA-104 (red line) reaches a true vertical depth (TVD) of 4346m (Elias Bahnan et al., 2020).

3.2 Petrography

Cement phases, fractures, veins, stylolites and cross-cutting relationships were recognized by using optical microscopy, cathodoluminescence and fluorescence. The microscope used for optical observations was a Zeiss© AX10 with a maximum magnification of x1000. A Cathodyne OPEA cold cathode instrument (400 mA and 13–15 kV gun current) in the GeoRessources Laboratory (Nancy, France) was used to perform cold cathodoluminescence (CCL) observations. Ultraviolet (UV) micro-fluorescence observations were made by using a Zeiss® AX10 optical microscope equipped with an HBO-100 epi-fluorescence source filtered at 365 ± 5 nm and an LP400 nm emission filter.

3.3 Isotope Geochemistry

3.3.1 Oxygen and carbon isotopes ($\delta^{18}O$ and $\delta^{13}C$)

For $\delta^{18}O$ and $\delta^{13}C$ analysis, 24 powder samples were collected with a DREMEL micro-drill from large veins to avoid mixing of several generations of cements during sampling. A Thermo-Scientific MAT253 isotope ratio mass spectrometer at CRPG laboratory (Nancy, France) was used for analysis. Measurements were calibrated using international standards IAEA CO-1, IAEA CO-8 and NBS 19. Values are reported in per mil (‰) relative to V-PDB (Vienna Pee Dee Belemnite). Reproducibility was checked by replicate analysis of standards and was ±0.07‰ (1 σ) for oxygen isotopes and ±0.01‰ (1 σ) for carbon isotopes. The oxygen isotopic compositions of the parent fluids ($\delta^{18}O_{water}$) were calculated by using the trapping temperatures obtained from fluid inclusion

149 modeling and the isotope fractionation equations for carbonates of O'Neil et al.(1969) for calcite
150 and Horita (2014) for dolomite.

151 3.3.2 Multiple sulfur isotopes ($\delta^{34}S$, $\Delta^{33}S$)

152 Multiple sulfur isotopes analysis ($\delta^{34}S$, $\Delta^{33}S$) was performed on two anhydrite samples drilled from
153 coarse anhydrite cements from the Upper Annelids formation. Sulfur from anhydrite was first
154 extracted by the acid attack technique using a Strongly Reducing Hydriodic Hypophosphorous acid
155 solution (STRIP; Kitayama et al., 2017) to release sulfur as H_2S which then reacted with silver
156 nitrate ($AgNO_3$) solution to precipitate silver sulfide (Ag_2S). The recovered Ag_2S was then reacted
157 with F_2 to produce SF_6 which was purified by cryogenic traps and gas chromatography. SF_6 was
158 then introduced into a ThermoFinnigan MAT 253 dual-inlet gas-source mass spectrometer. These
159 analyses were carried out at the Institut de Physique du Globe de Paris (IPGP, France). All data
160 are reported in the classical $\delta^x S$ notation (with x = 33 or 34) and expressed in ‰ with respect to the
161 Vienna Cañon Diablo Troilite (V-CDT) standard. Capital delta (Δ) notation is used to represent $\delta^{33}S$
162 deviations from a reference line (Hulston and Thode, 1965) defined as:

163 $$\Delta^{33}S = \delta^{33}S - 0.515 \times \delta^{34}S \qquad (1)$$

164 Standard deviation is better than 0.1‰ and 0.01‰ for $\delta^{34}S$ and $\Delta^{33}S$, respectively.

165 3.3.3 U/Pb isotopes

166 To obtain absolute ages on diagenetic phases using U/Pb isotopes, the Laser Ablation-Inductively
167 Coupled Mass Spectrometry (LA-ICPMS) technique was used on dolomite and calcite cements.
168 The analyses were done at the GeoRessources Lab in Nancy, France. Laser sampling was
169 performed with a 193 nm GeoLas Pro ArF Excimer laser equipped with beam homogenization
170 optics. The ablation beam was focused at the sample surface with a constant fluency of 10 J/cm^2.
171 The repetition rate was stabilized at a frequency of 5 Hz. Helium was then used as a carrier gas to
172 transport the aerosols, released from the targeted sample spot, from the ablation cell to the
173 spectrometer. These aeorsols were analyzed by an Agilent 7500c Quadrupole ICP-MS equipped
174 with an Octopole Reaction System and an enhanced sensitivity lens (Cs type, Agilent). The
175 certified glass standards NIST610, NIST612 and NIST614 SRM were used as reference materials
176 (concentrations from Pearce et al. (1997) for the calibration of the LA-ICP-MS.

3.4 Fluid inclusion microthermometry

Microthermometric measurements were carried out on a Linkam THMS600 heating-cooling stage connected to an Olympus BX51 microscope, at the GeoRessources Lab (Nancy, France). Glass-mounted rock slices of nearly 120 µm thickness were prepared at the litho-preparation unit of the GeoRessources Lab, Nancy. The finished slices were then soaked in acetone for 24 hours to dissolve the glue and unmount the rock samples from the glasses. It is important to note the all samples were prepared under running cold water to avoid pre-heating the samples before microthermometry. Synthetic H_2O pure fluid inclusion standard and a natural aqueous fluid inclusion standard (Ta 33.2) were used for calibration. The phase transition temperatures (i.e. homogenization into the liquid phase) have an accuracy of about ±0.2°C, and the obtained data were calibrated accordingly. When the inclusions were too small (less than 5 µm) the glass cover was removed to allow better visibility but the error range increased to up to +1.5°C. Individual rock slices were petrographically observed before being cut down to small chips. To avoid heating other fluid inclusions, the chips were broken down to small sizes to allow one field of view per sample to be studied. Individual fluid inclusions were manually drawn and traced on a copybook to make it easier to trace their location at different depths within the field of view. Homogenization temperatures were recorded in an ascending order after gradually heating the chip at a rate of 2°C/minute. At each temperature increase increment, all selected fluid inclusions were observed and checked for the homogenization of the vapor phase. When the gas phase, the bubble, was too small to observe, the cycling procedure was employed to check for homogenization. After homogenization recording was done, freezing cycles were carried out to record the final ice melting temperatures (Tm_i). Tm_i was converted to equivalent mass % NaCl following the equation of Bodnar (1993). In total, 207 aqueous fluid inclusions and 167 oil inclusions were analyzed, distributed over 3 dolomite samples, 4 calcite samples and 3 anhydrite samples. The choice of these samples was done after a preliminary scan of nearly 80 thin sections, after which those of representative cross-cutting relationships between the diagenetic phases, as well as coarse crystal phases were selected for the FI study.

3.5 Raman spectroscopy

Raman spectroscopy was used to analyze the gases dissolved in the aqueous fluid inclusions. In samples where the melting temperature was not easily measured, the salinity of the aqueous phase was determined by a calculating the area under the Raman band of the water stretching vibrations, which is influenced by the presence of chloride ions (Caumon et al., 2015). Analyses were performed with a LabRAM HR spectrometer (Horiba Jobin Yvon) equipped with a 600 $g.mm^{-1}$ grating and an Edge filter. The confocal aperture was 200 µm and the slit aperture was 200 µm. The excitation beam was provided by a Stabilite 2017 Arþ laser at 457.9 nm to 514.5 nm with a power of 200 mW. The acquisition time was 20 seconds x10 accumulations to optimize the signal-to-noise ratio. Quantification of the CH_4 was done following the best fit, second-order polynomial curve obtained from the calibrations of Caumon et al. (2015). The uncertainty on the calculated CH_4 molality value resulting from the calibration function (±1σ) is less than ±2% (Caumon et al., 2014). The area ratios were calculated by using the integral tool in LabSpec. The spectra with peaks between 2550 and 2600 cm^{-1} were analyzed to quantify the concentration of HS^- (2570 cm^{-1}) and H_2S (2590 cm^{-1}). To quantify the ratios of these species, the Raman spectra were treated using the *Opus (Bruker)* software. After baseline correction, the spectra were decomposed by using the Levenberg-Marquardt algorithm to differentiate the HS^- and H_2S species. Concentration of sulphur aqueous species were calculated following the outline of Jacquemet and Pironon (2006).

3.6 Fluid modeling

Aqueous inclusions thermodynamic (AIT) modeling is a calculation procedure that relies on the homogenization temperature and the chemistry of the aqueous fluid phases to draw the pressure-temperature phase diagrams using an Equation of State (EoS). Similarly, petroleum inclusions thermodynamic (PIT) modeling allows the construction of phase diagrams of petroleum inclusions. The intersection of isochores of aqueous and oil inclusions, known as the double-isochore technique (Bourdet et al., 2008) indicates the trapping P-T conditions of fluids. Given limitation in detecting the exact quantity of H_2S dissolved in the oil inclusions, 2 compositions of oil inclusions are modeled, such that the first has 0% H_2S while the second has 20% H_2S. These two compositions allow the modeling of the minimum and maximum possible compositions. To date, no EoS exist that can model the phase evolution of a fluid system composed of H_2O-NaCl-CH_4-H_2S-HS^- at temperatures less than 200°C. Hence, a workflow is developed that can take into account

235 the impact of H_2S on the homogenization pressure (P_h) and which can be extrapolated to the P-T
236 domain of the studied fluid inclusions. After obtaining the composition of the aqueous phases using
237 Raman spectroscopy (section 3.5), the EoS of Duan and Mao (2006) was used, which is suitable
238 to model fluids containing CH_4-H_2O-NaCl at temperatures between 0-275°C pressures of 1-2000
239 bars. With this EoS, the homogenization pressure (P_{h1}) was obtained (step 1 – table 1). The
240 obtained P_{h1} was then added to the P_h obtained from the EoS of Zhang and Frantz (1987) hereby
241 labeled $P_{hz\text{-}f}$ (step 2 – table 1). This EoS is commonly used to draw isochores between 0-700°C
242 and pressures up to 3000 bars for the H_2O-NaCl fluid system. Adding P_{h1} to $P_{hz\text{-}f}$ gives P_{h2} and
243 allows the construction of the isochores of CH_4-bearing fluids without the impact of H_2S (step 3 –
244 table 1). To model the influence of H_2S on the isochores, Loner 9 software
245 (http://fluids.unileoben.ac.at/Computer.html), which relies on the EoSs of (Duan et al.,1992a,b;
246 1996) was used. These EoSs allow the modeling of H_2O-CO_2-CH_4-H_2S fluids systems but at
247 temperatures higher than the supercritical and pressures up to 25000 bars. Since the validity
248 domain is beyond the temperature range of the fluid inclusions, simulations were made at T=250°C
249 which rendered a valid solution in the thermodynamic modeling of the Loner 9 software. The
250 purpose of this calculation step is to analyze the difference in homogenization pressures with and
251 without H_2S. This step gave P_{h3} that shows the homogenization pressure of an H_2S-bearing fluid at
252 250°C (step 4 – table 1). However, since the EoS of Duan and Muao (2006) was used to draw the
253 isochore of fluids without H_2S and to be consists when comparing different isochores with or
254 without H_2S, the EoS of Duan and Muao (2006) was again used to calculate another
255 homogenization pressure P_{h4} at T=250°C (step 5 – table 1). P_{h4} is similar to the P_{h1} with the
256 exception of the higher temperatures. The purpose of calculating both P_{h3} and P_{h4} is to compare
257 how H_2S changes the P_h of a fluid that homogenized at T=250°C. ΔP_h is then the difference
258 between P_{h3} and P_{h4} such that $\Delta P_h = P_{h3} - P_{h4}$ (step 6 – table 1). To be able to model the fluids at
259 their real homogenization temperatures and with the impact of H_2S, i.e. with ΔP_h, P_{h4} is calculated
260 as $P_{h4} = P_{h1} + \Delta P_h$ (step 7 – table 1). Finally, a second isochore is constructed by adding P_{h4} to the
261 $P_{hz\text{-}f}$ (step 8 – table 1). These calculation steps are summarized in table 1.

262 Table 1. Workflow showing the calculation steps and their purposes for the AIT modeling.

Step	Parameters	T (°C)	EoS used	Validity range	Purpose	Gases present
1	P_{h1}	T_h	Duan and Muao (2006)	T=0-275°C P=1-2000 bars	Impact of CH_4 on P_h	CH_4
2	$P_{hz\text{-}f}$	T_h	Zhang and Frantz	T=0-700°C	Construction of isochores	None

			(1957)	P=0-3000 bars		
3	$P_{h2} = P_{h1} + P_{hz\text{-}f}$	T_h	Zhang and Frantz (1957) + P_{h1}		Construction of isochores	CH_4
4	P_{h3}	250°C	Duan et al. (1992a,b; 1996)	T>supercritical P=0-25000 bars	Impact of CH_4+H_2S on P_h	CH_4+H_2S
5	P_{h4}	250°C	Duan and Muao (2006)	T=0-275°C P=1-2000 bars	Impact of CH_4 on P_h	CH_4
6	ΔP_h (P_{h3} - P_{h4})	250°C			Impact of H_2S on P_h	CH_4+H_2S
7	$P_{h4} = P_{h1} + \Delta P_h$	T_h			Impact of CH_4+H_2S on P_h at T_h	CH_4+H_2S
8	$P_{h5} = P_{hz\text{-}f} + P_{h4}$	T_h	Zhang and Frantz (1957) + P_{h4}		Construction of isochores	CH_4+H_2S

The modeling workflow assumes that the difference in P_h remains constant when extrapolating from 250°C to the measured T_h. This assumption is validated by calculating the homogenization pressures again at 300°C, which showed constant difference between the two data sets. With this consistency, it is assumed that the part of the isopleth at 250°C is a straight line and the extrapolation from 250°C to the measured T_h remains along this straight line. Therefore, after adding H_2S to the fluid system, the new isopleth is expected to be parallel and hence adding P_{h1} to ΔP_h can be justified.

Petroleum inclusions thermodynamic modeling (PIT) allows the construction of the P-T phase diagram of a petroleum inclusion. This was done by obtaining a 3D volumetric reconstruction of oil inclusions to determine the bubble point curves and eventually the phase diagrams. These 3D images were obtained by compiling stacks of images captured using a Confocal Scanning Laser Microscope (CSLM) fitted with a Biorad Rainbow system adapted to a Nikon inverted microscope at the GeoRessources Lab (Nancy, France). Emission source was an Argon laser at 488 nm and a diode laser at 405 nm. Observations were done through an oil-immersed 60x objective lens. This method allows volume estimation of the cavity of a petroleum inclusion with an accuracy greater than 95%. The x–y resolution was 0.2 µm and the resolution along the z-axis was approximately 0.5 µm. The studied chips were glued on a glass plate using paraffin to avoid any movement during acquisition. For a higher accuracy, the radii of the gas phases in oil inclusions were measured prior to CSLM measurements by using optical light microscopes. To construct the phase diagrams, the PIT modeling software developed by Thiéry et al. (2002) was used. To model the impact of H_2S on the isochores of oil inclusions, and given the limitations in accurately quantifying H_2S dissolved in oil inclusions using infrared spectroscopy, two isochores of each oil inclusion are

286 modeled; one containing 0% H_2S and the other 20% H_2S. These two compositions represent
287 geologically reasonable end-members and can help in placing a range of trapping P-T conditions.

288 # 4 Basin Modeling

289 The geodynamic history of the Lacq petroleum system was modeled using Petromod 1D software.
290 A synthetic well combining the entire stratigraphy of wells LA-101 and LA-104 was prepared from
291 drilling reports and used as the main input source for the model. Boundary conditions were set by
292 using the paleowater depths (PWD), sediment-water interface temperatures (SWIT) and basal heat
293 flow (HF) as discussed by Elias Bahnan et al. (2020). Vitrinite data were collected from TOTAL
294 archives and were used to calibrate and validate the thermal history of the model.

295 # 5 Results

296 ## 5.1 Petrography of diagenetic phases

297 Precursor limestones consist of chalky mudstones, wackestones to bioclastic packstones (Fig. 4-A
298 and B). Bioclastic material consists of microforaminifera, shells of mollusks, sponges, echinoderms
299 and annelids, with sizes reaching up to 2 mm.

300 ### 5.1.1 Micritization

301 Microborings filled by micrite growing from the walls of the bioclasts inwards are observed (Fig. 4-
302 A). This phenomenon, in some cases, is widespread enough to engulf the entire bioclast and
303 hence disrupts the original structure of the grain.

304 ### 5.1.2 Pyrite

305 Clusters and agglomerates of rounded, to sub-rounded framboidal pyrite crystals are observed on
306 shells and bioclastic fragments and inside bioclastic micropores (Fig. 4-B). Individual crystal sizes
307 range between few µm up to nearly 40 µm. Under reflected light microscopy, a golden yellowish
308 color, typical of pyrites, is observed (Fig. 4-B).

309 ### 5.1.3 Dolomite 1

310 This dolomite phase is represented by rhombohedral dolomite crystals with average crystal sizes
311 between 30 and 80 µm (Fig. 4-C). CCL microscopy reveal a dark core and a bright yellow to

orange luminescent external rim. The core of some crystals is dissolved thus creating intra-crystalline secondary porosity.

5.1.4 Dissolution

Moldic porosity, later infilled by other cements (Fig. 4-D), provide indirect evidence that dissolution may have occurred before cementation. This dissolution phase is also evidenced by the corroded rims and dissolved cores of the Dol. 1 phase (Fig. 4-C).

5.1.5 Calcite 1

This is a diagenetic phase limited to the Annelids Limestone Formations. It appears as zoned dog-tooth to columnar calcite cements lining the walls of moldic pores (Fig. 4-D and E). Under CCL, zoning evolve from a dull-orange/brown core to progressively brighter orange to yellow colors (Fig. 4-E). Crystal sizes range between 5 and 30 µm. Zoning is well-developed and show no evidence of recrystallizations. No aqueous or oil inclusions are observed in this phase.

5.1.6 Calcite 2

This second calcite phase appears as a yellow-orange overgrowth engulfing the dog-tooth calcites of the Annelids Limestone Formations. The crystals are coarse (~300µm), equant and have sub-rounded terminations which helps to distinguish them from other calcite phases. Under CCL, no zoning is observed and crystals are characterized by uniform shades of yellow to dull orange colors with no evidence of recrystallization (Fig. 4-E). When this phase develops in open vuggy pores, crystal-sizes can reach up to 650 µm. No aqueous or oil inclusions were observed in this phase.

5.1.7 Mechanical compaction

This episode is represented by the collapse of the rounded bioclasts and shell fragments. Figure 4-F shows an example of an annelid stem that has undergone mechanical compaction as witnessed by the damage of its walls.

5.1.8 Stylolite 1

337 This is a minor compaction phase represented by low-amplitude stylolites with a horizontal
338 orientation parallel to the stratigraphy. These stylolites are cross-cut by calcite/dolomite-infilled
339 fracture A1 (Fig. 5-A).

340 5.1.9 Fracture A1

341 Fractures A1 cross-cut the host rocks and stylolites 1 (Fig. 5-A) and are characterized by straight
342 walls with thicknesses between 5µm up to 3cm. Infilling cements are composed of saddle dolomite
343 and calcite.

344 5.1.10 Dolomite 2

345 In the fracture set A, very coarse dolomite crystals, reaching up to 3mm in size, with curved faces
346 are observed (Fig. 5-B). They have turbid cores and growth zones rich in fluid inclusions. Oil
347 inclusions are also identified in the growth zones. CCL microscopy reveal a zoned core with
348 luminescence alternating between different shades of red. In some cases, the dolomite 2 phase,
349 known as saddle dolomites, is partially replaced by a calcite phase (Fig. 5-B).

350 5.1.11 Fracture A2

351 The occurrence of host-rock fragments inside fractures A (Fig. 5-B) sealed by the calcite 3
352 cements suggests a fracturing mechanism during or prior to the cementation of the calcite 3.

353

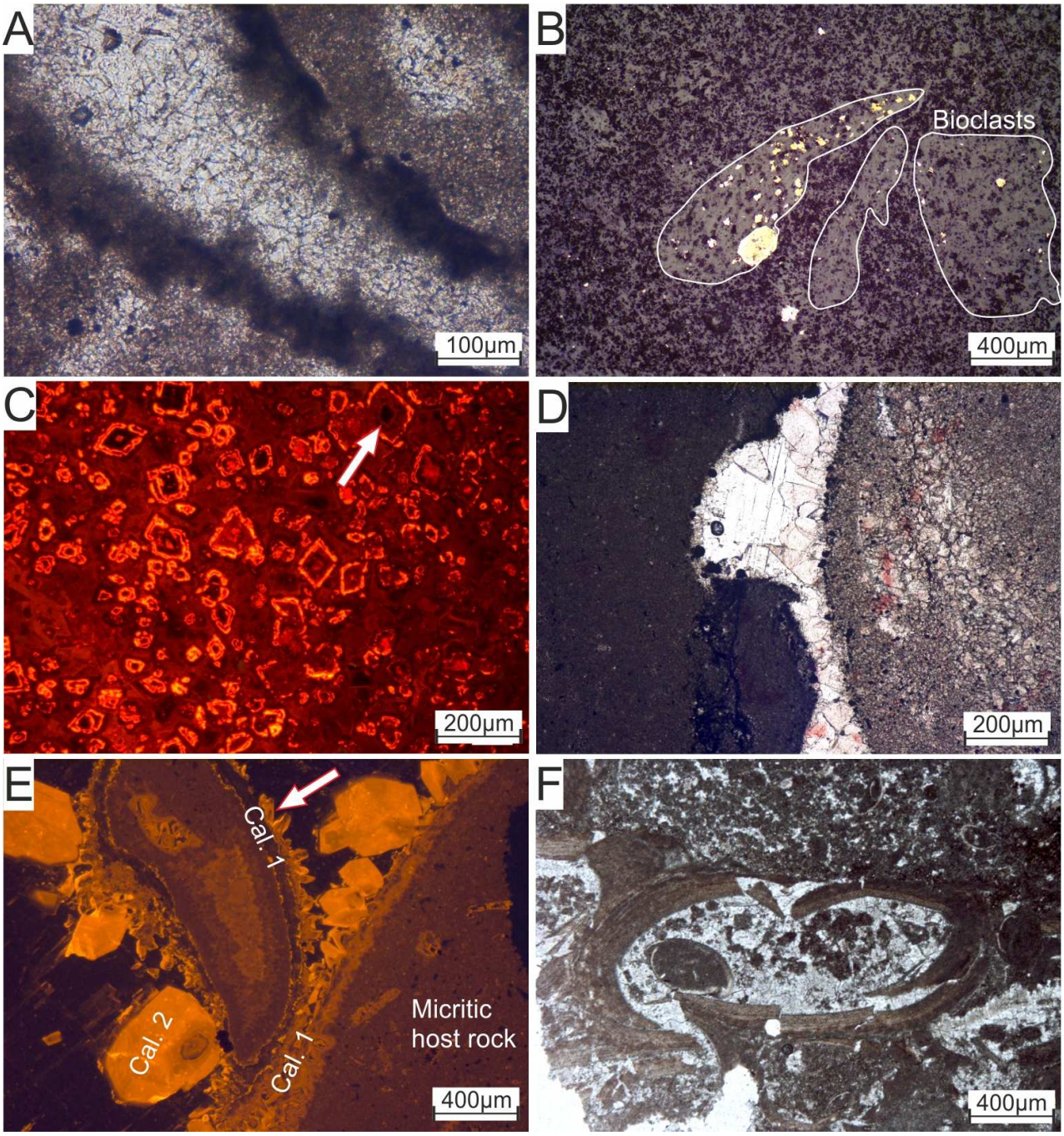

Figure 4. A: Plane polarized light (PPL) image of a shell fragment affected by destructive micritization. The shell is later replaced by other calcite phases. B: reflected light image showing ghosts of bioclasts with local concentrations of rounded to sub-rounded pyrites. C: CCL image of partially dissolved rhombic dolomite crystals with a brightly luminescent external rim. Arrow point to a dissolved core within a crystal. D: shell mold cemented by calcite and anhydrite cements. This shell was initially dissolved and moldic porosity was filled by younger cement phases. E: CCL image of the zoned "dog-tooth" calcite 1 phase precipitated at the contact with the host rock and covered by the yellow-luminescent calcite 2 phase. F: Broken annelid tubes as evidence of mechanical compaction.

5.1.12 Calcite 3

This dominant cement phase occludes most of the fracture and vuggy porosity (Fig. 5-C) and significantly reduces reservoir quality. These calcites are drusy with crystal-sizes reaching up to 8 mm (Fig. 5-D). Lack of uniform CCL zoning and the heterogeneous brown to dull orange colors

suggest possible recrystallization. Relics of saddle dolomites are frequently observed in Calcite 3 (arrows in fig. 5-D). This phase is rich in oil and aqueous inclusions.

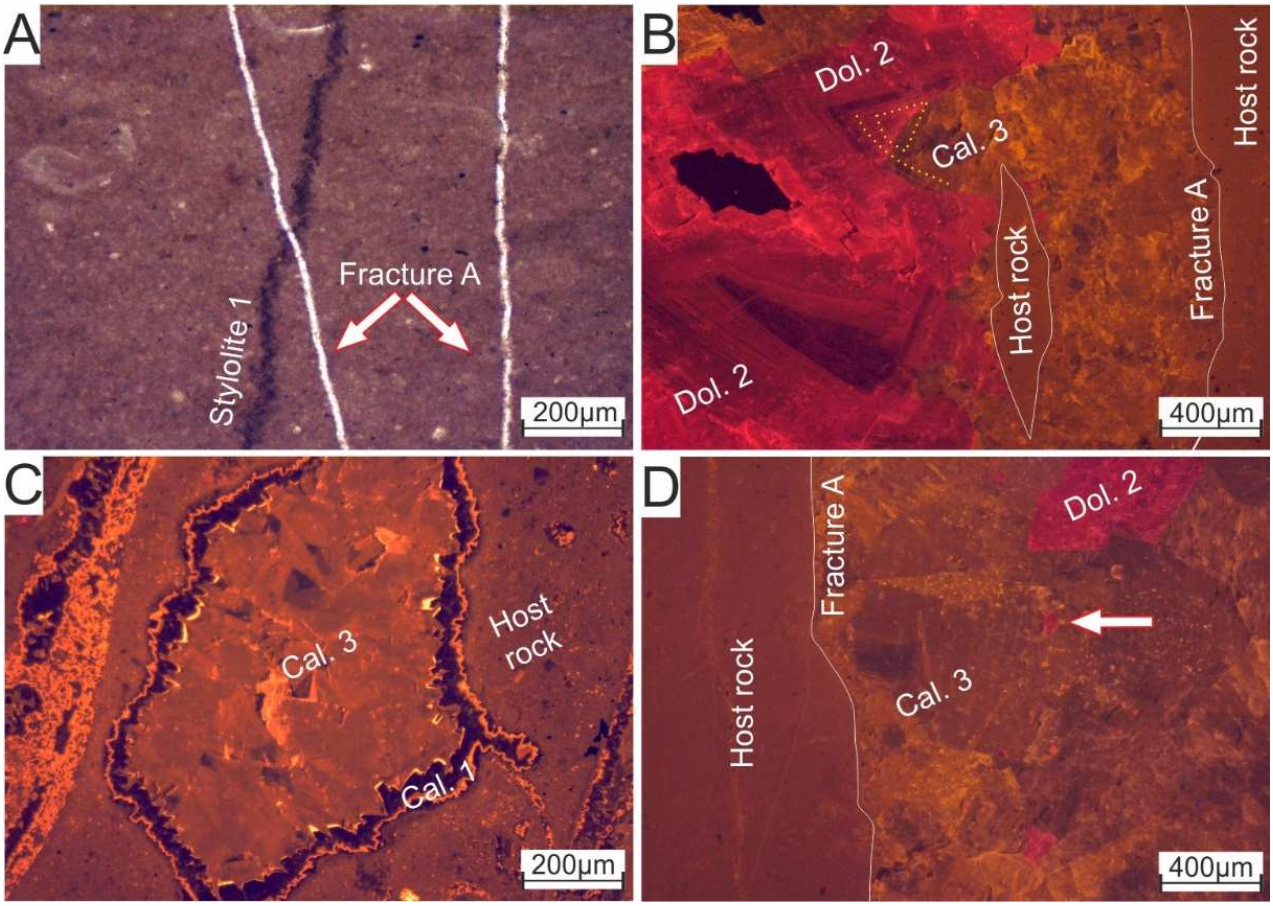

Figure 5. A: PPL photomicrograph of stylolite 1 crosscut by fracture set A. B: CCL image of the cross-cutting relationships between fracture A, dolomite 2 and calcite 3 phases. Fragments of host rocks in the fracture are indicators of fracture reopening mechanism. Dolomite 2 is partially replaced by calcite 3 (see the yellow dotted line between Dol. 2 and Cal. 3). C: CCL image of a vuggy pore now filled by Cal. 1 and Cal. 3 calcites. D: CCL image of coarse calcite 3 crystals. Arrows indicate remnants (relics) of Dol. 2 after replacement. Cal. 3 shows heterogeneous shades of yellow to dull orange luminescence.

5.1.13 Fracture B

Fracture set B postdates calcite 3 and is filled by anhydrite. The width of fractures can reach up to 1cm (arrows in Fig. 6-A) and appear mostly as vertical fractures when viewed at the macroscopic scale.

5.1.14 Anhydrite

Anhydrite was observed inside the vertically oriented fracture set B in wells LA-101 and LA-104 (Fig. 6-A) and tend to form massive nodules and concretions that replace the initial fabrics of the host lithology. The thickness of anhydrite layers, observed in the studied cores (Fig. 6-A) can reach up to 50cm. Stratigraphically, the massive anhydrites lie immediately under the Sainte-Suzanne marls where they partially replaced the Upper Annelids Limestone Formation, and reach around 15

to 20 meters in total thickness. This phase also occurs as pore-blocking cements in all the studied formations. Under plane polarized light (PPL), anhydrites appear clear white to creamy, while under cross-polarized light (CPL), an array of bright second order colors were observed (Fig. 6-B, C and D). This is the last diagenetic cement that replaces younger calcite and dolomite phases. No luminescence was detected under CCL. Similarly, under PPL, crossed-polarized light (CPL) and CCL, no evidence of gypsum precursor was observed. Several morphologies of anhydrites have been identified.

1. Coarse and tabular crystals with sizes reaching up to 2 mm (Fig. 6-B and D), often showing evidences of calcite and dolomite replacement (Fig. 6-C), and rich in oil and aqueous inclusions.
2. Fine fibrous crystals filling nodules inside the host rocks. Fracture set B is often observed connected to these nodules (Fig. 6-B). Individual crystal size is no more than 50 µm (Fig. 6-B). These are too small to observe aqueous or oil inclusions.

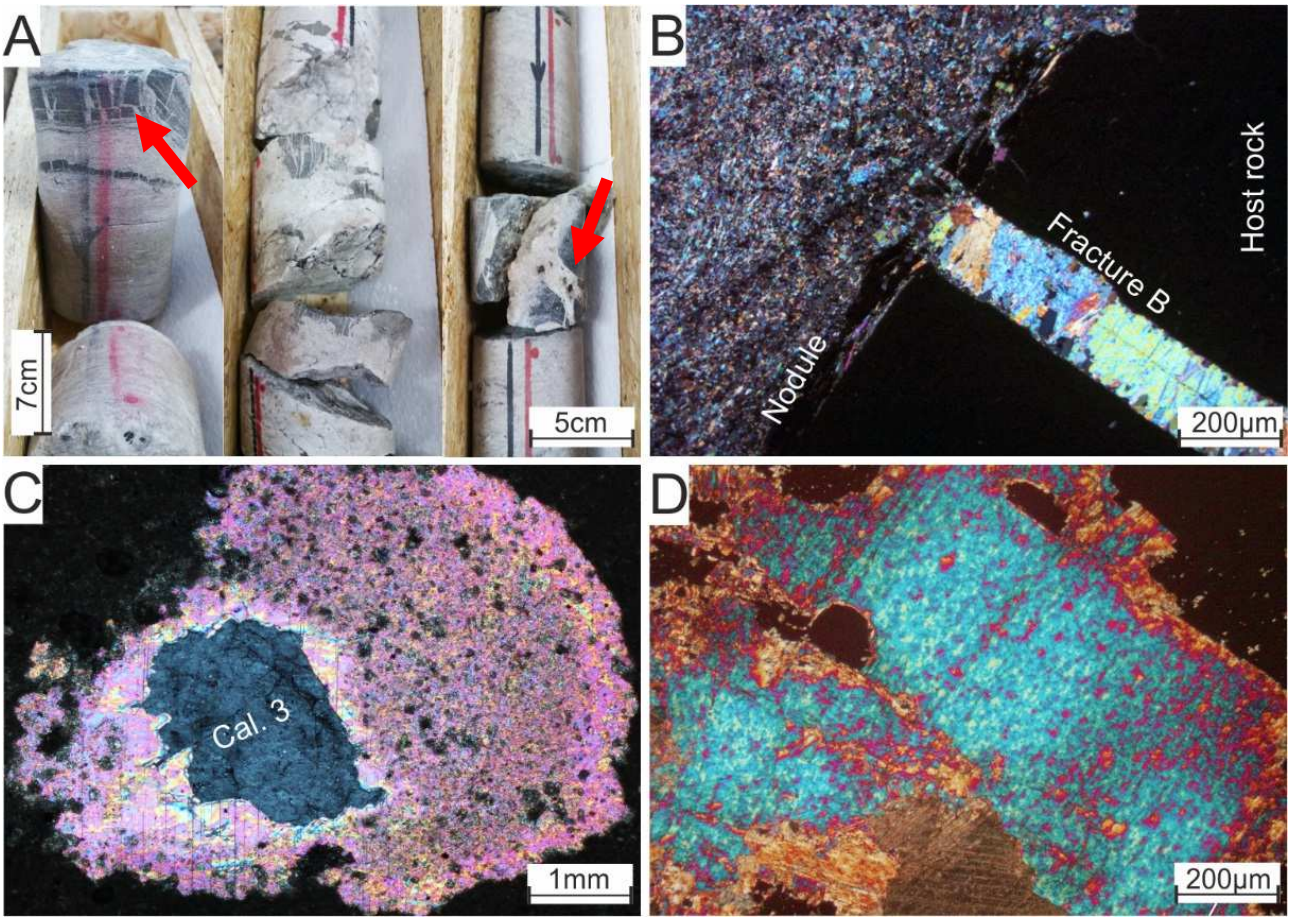

Figure 6. A: Photographs of well LA-101 and LA-104 with massive anhydrites few meters below the Sainte Suzanne Formation. Arrows point to cm-scale veins. B: CPL image of an anhydrite-filled fracture C in a host micrite matrix in contact with an anhydrite nodule. C: CPL image of an anhydrite with partial replacement of a calcite 3 crystal. D: CPL image of coarse anhydrite crystals with bright 2nd order birefringence.

5.1.15 Stylolite 2

These stylolites have amplitudes in the range of 200 to 600µm, are mostly oblique relative to the vertical wells and crosscut anhydrites (Fig. 7-A).

5.1.16 Fracture C

This last fracturing phase affected all previous phases and generated fracture porosity in the reservoir of Deep Lacq. The fracture set C crosscuts calcite-filled fracture A (Fig. 7-B) and anhydrite-filled fracture B (Fig. 7-C).

5.1.17 Dissolution

A final phase of dissolution is represented by solution-enhanced fractures that enlarged fracture set C (Fig. 7-C) where in some cases it created vuggy porosities (Fig. 7-D).

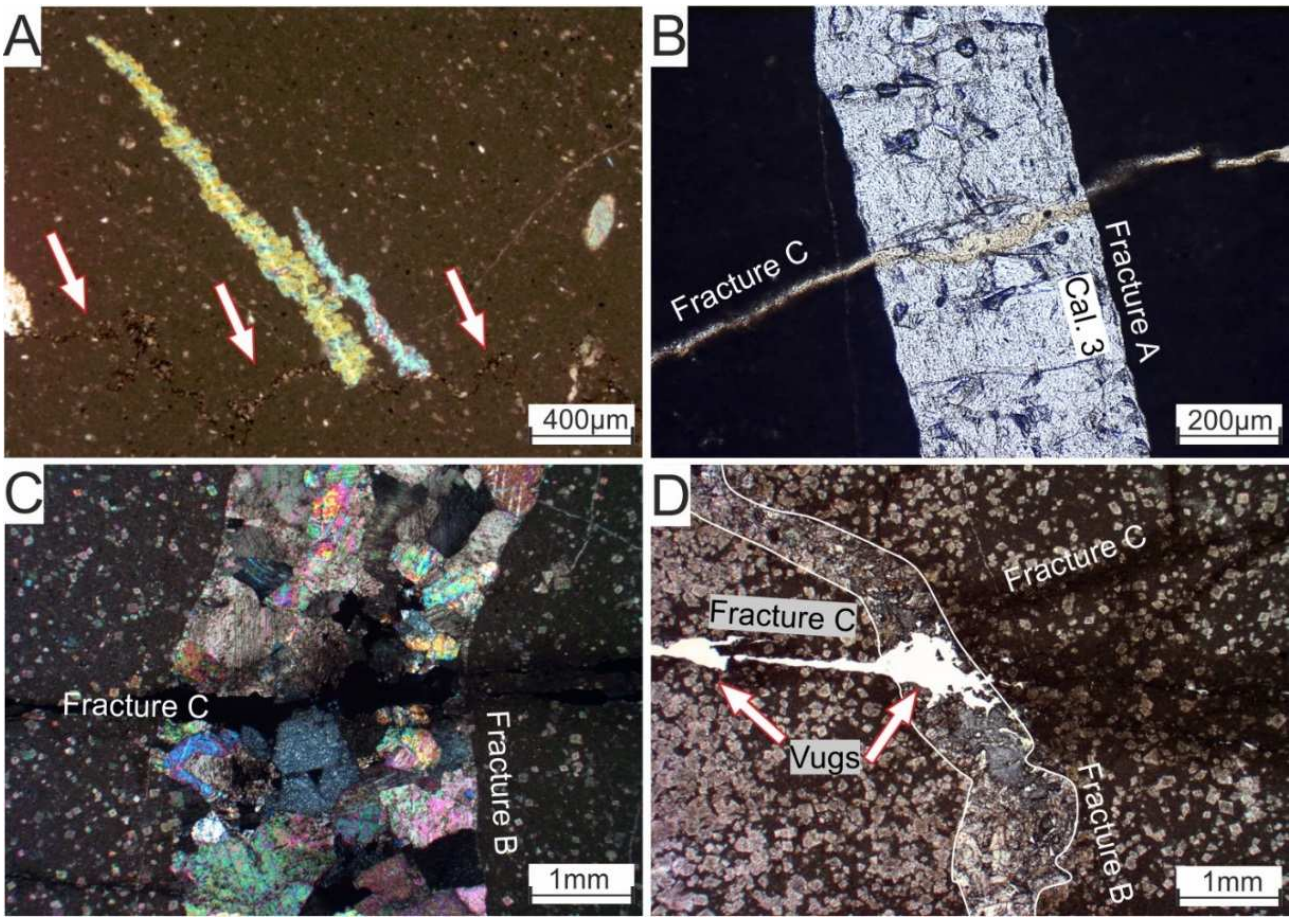

Figure 7. A: CPL photomicrograph of anhydrite affected by stylolite 2 (arrows). B: PPL image of a fracture A filled by calcite (Cal. 3) crosscut by an open fracture C. C: Anhydrite-infilled fracture B crosscut by fracture C. D: Fracture B crosscut by a fracture C with a solution-enhanced vuggy-porosity.

5.2 Isotope Geochemistry

$\delta^{18}O$ and $\delta^{13}C$ isotopes were obtained from the micritic host rocks (n=10), Dol. 2 (n=4) and Cal.3 (n=10) cements (Fig. 8) of the Lons, Algal and the Annelids formations. $\delta^{13}C$ of the host black mudstones are in the range of -2.4‰ to +2.5‰ PDB and $\delta^{18}O$ between -3.7‰ to -0.6‰ PDB. Dol. 2 have $\delta^{13}C$ values between +5.5 and +5.6 ‰ PDB and a depleted $\delta^{18}O$ between -6 and –6.2 ‰ PDB. $\delta^{13}C$ of calcite 3 is between +1.6 and +4.3 ‰ PDB while $\delta^{18}O$ varies between -2.8 and -5.6 ‰ PDB. Error ranges for individual data points are within the symbols plotted in figure 8 and are between ±0.01 to ±0.07 (1σ) from the reported values.

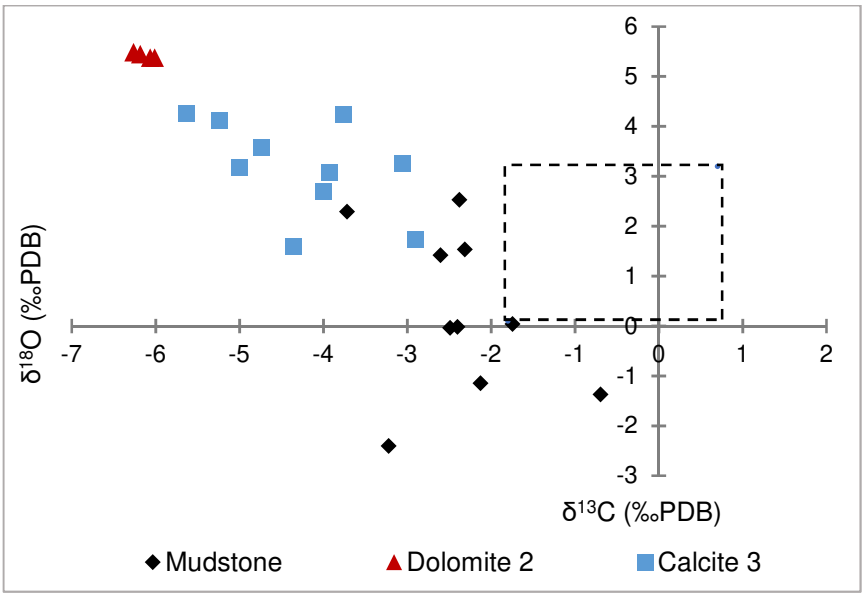

Figure 8. Cross-plot of $\delta^{18}O$ and $\delta^{13}C$ isotopes for Deep Lacq. Dashed box represents the Late Jurassic seawater signature (Veizer et al., 1999).

The two analyzed anhydrites from the Annelids formation were sampled from massive anhydrites at 3514.5 m (well LA-104) and 3619.5 m (well LA-101) and they respectively show multiple sulfur isotopes signatures at: $\delta^{34}S$ = 19.12‰ ±0.006, $\Delta^{33}S$ = 0.023‰ ±0.009 and $\delta^{34}S$ = 18.97‰ ±0.005, $\Delta^{33}S$ = 0.017‰ ±0.011. The error range represents 1σ for dual-inlet mass-spectrometry measurements. These values are consistent with signatures observed in the Keuper carbonate associated sulfates (CAS) at $\delta^{34}S$ = 20.6‰ ±5.4 and $\Delta^{33}S$ = 0.000‰ ±0.025 (Wu et al., 2010 – 2014).

The detected amounts of U and Pb in calcite and dolomite samples ranged between 0.001 and a 0.004 ppm. Of the 52 measurements, 18 were below the detection limits of the spectrometer. These quantities of U and Pb are too low to meet the minimum pre-requisites for U/Pb geochronology and hence proceeding with this step was not possible.

5.3 Fluid inclusions

5.3.1 Petrography

The Dol. 2, Cal. 3 and Anhydrite are the coarsest cement phases in Deep Lacq with fluid inclusions of suitable sizes allowing proper observations and analyses.

In Dol. 2 crystals, two-phase aqueous inclusions and two-phase oil inclusions are observed along growth zones (Fig. 9-A and B). The aqueous inclusions have mostly irregular to oval shapes with sizes ranging between 3 to 8 µm. These aqueous inclusions are located close to two-phase light brown oil inclusions which, when viewed under UV light, display a strongly fluorescent blue to white color (SD-O-1-2 in Fig. 9-B). The liquid/vapor ratio noted as Fv%, of these studied inclusions was visually assessed and approximated to nearly 8%. Fv% is constant across all studied FIs in the dolomite phase.

Special attention was given to check for possible necking down or post-entrapment alteration of the fluid inclusions. A necked-down inclusion would typically appear as a split-up inclusion between a single-phase aqueous inclusion and a smaller inclusion dominated by the vapor phase (Diamond and Tarantola, 2015). No petrographic evidence was found of such inclusion or possible intermediate inclusions in the process of being necked down.

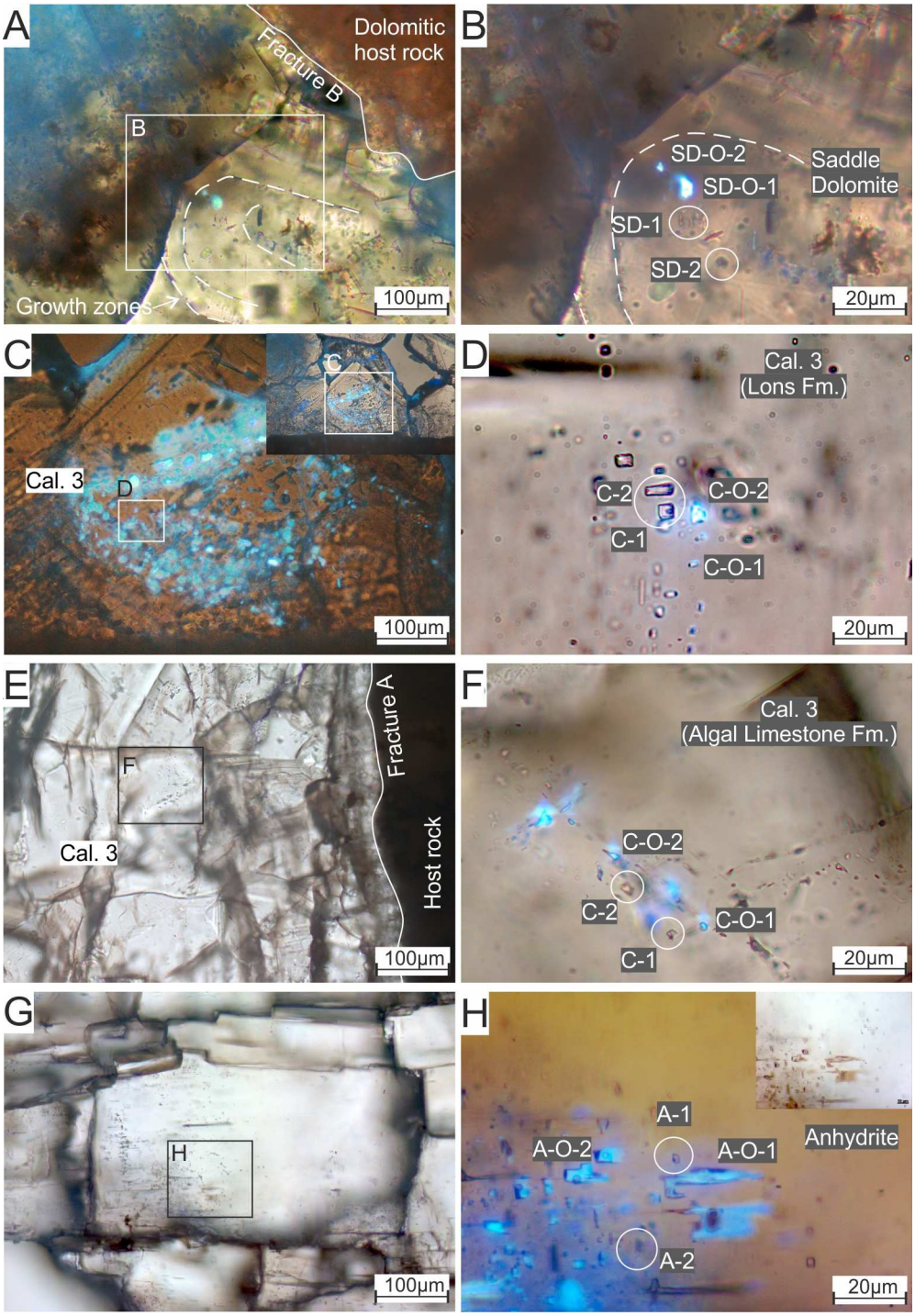

Figure 9. A: Coarse dolomite 2 crystal with oil and aqueous inclusions. The growth zones are traced in the dashed white lines B: The oil inclusions SD-O-1 and SD-O-2 show a strongly fluorescent blue to white color. White ovals contain two-phase aqueous inclusions SD-1 and SD-2. C: Aqueous and blue-fluorescent oil inclusion in Cal 3 of the Lons Limestone formation. The assemblage where the aqueous and oil inclusions are found terminate before the edge of the crystal and does not indicate continue to other crystals. D: Blue fluorescent oil inclusions (C-O-1 and C-O-2) and aqueous inclusions (C-1 and C-2). E: Fluid inclusions in Cal. 3 of the Algal Formation. F: Blue fluorescent oil inclusions (C-O-1 and C-O-2) and aqueous inclusions (C-1 and C-2). G: Photomicrograph of an anhydrite crystal with a cluster of aqueous and oil inclusions. Each anhydrite crystal has its own cluster of inclusions, none with clusters extending to other crystals. H: UV light showing the strong blue color of oil inclusions (A-O-1 and A-O-2) adjacent to the two-phase aqueous inclusions (A-1 and A-2).Notice the brown PPL color of the oil inclusions, different from those trapped in the saddle dolomites and calcite phases .

In the Cal. 3 cement, two-phase aqueous inclusions are identified in clusters limited to individual crystals (Fig. 9-C, D, E and F) These aqueous inclusions have inverted geometries, rectangular, oval and irregular shapes with sizes ranging from 5 up to 70 µm. The oil inclusions have a strongly

fluorescent blue to white colors under UV light (Fig. 9-D and F). The Fv% of the aqueous phases was consistent and ranged between 9-10% across all observed inclusions in the calcites

Two-phase primary aqueous and oil inclusions are observed in the coarse anhydrite crystals. The aqueous inclusions have cubic to rectangular shapes with relatively small sizes in the order of 5-15 µm (Fig. 9-E). Oil inclusions in anhydrites are two-phased, with brown to orange color under PPL and strong blue fluorescence under UV (Fig. 9-H). They have elongated rectangular to inverted geometric shapes. These inclusions are observed in clusters within crystals. The clusters are confined to individual crystals and do not extend to nearby cements. Similar to the case of the FIs trapped in the dolomite and the calcite phase, the Fv% of all studied aqueous inclusions was consistent and approximated to around 10%.

5.3.2 Microthermometry

The studied sample of Dol. 2 was retrieved from the Mano Dolomite Formation at a depth between 3707-3715 m. The aqueous inclusions homogenized into the liquid phase at a T_h range of 132-148°C with a mode T_h at 144°C (Fig. 10-A). The oil inclusions also homogenized into the liquid phase at a T_h range of 80-98°C with a mode T_h at 88°C (Fig. 10-A). After freezing down to -100°C, phase changes were observed and the final melting ice temperatures were detected. Only two reliable Tm_i were recorded between -6.8 and -5.2°C that correspond to salinities of 8.2 and 10.2 eq. wt.% NaCl respectively (Fig. 10-B).

Three samples of Cal. 3 were studied from the Lons Formation (4116m), the Annelids formation (3488 m) and the Algal limestone formation (3627 m). In the Lons formation, one population of two-phase aqueous is observed with a T_h range of 106-110°C with a T_h mode at 108°C (Fig. 10). This population was observed in clusters and its association to growth zones was not possible with confidence, as seen in figure 9-C. These aqueous fluid inclusions have salinities between 12 and 13 wt.% NaCl and are present with a dominant oil inclusion phase that homogenized at a T_h range of 50-66°C with a mode T_h at 56°C.

In the Cal. 3 samples of the Algal Limestone formation, two populations of two-phase aqueous inclusions are present. The first was observed along growth zones and homogenized into the liquid phase at a T_h range of 118-142°C with a mode at 126°C (Fig. 10-E). The population of two-phase oil inclusions is petrographically associated with this primary FI population. The second population

was observed along clusters or groupings whose association to growth zones could not be robustly established. This second population also homogenized into the liquid phase but at a lower T_h range of 94-104°C with a mode of 100°C. Both populations of aqueous inclusions have similar salinities measured from both the final ice melting temperatures and the Raman spectra. Tm_i was recorded between -7 and -9 °C that corresponds to a range of salinities of 11- to 13 eq. wt.% NaCl respectively (Fig. 10-F).

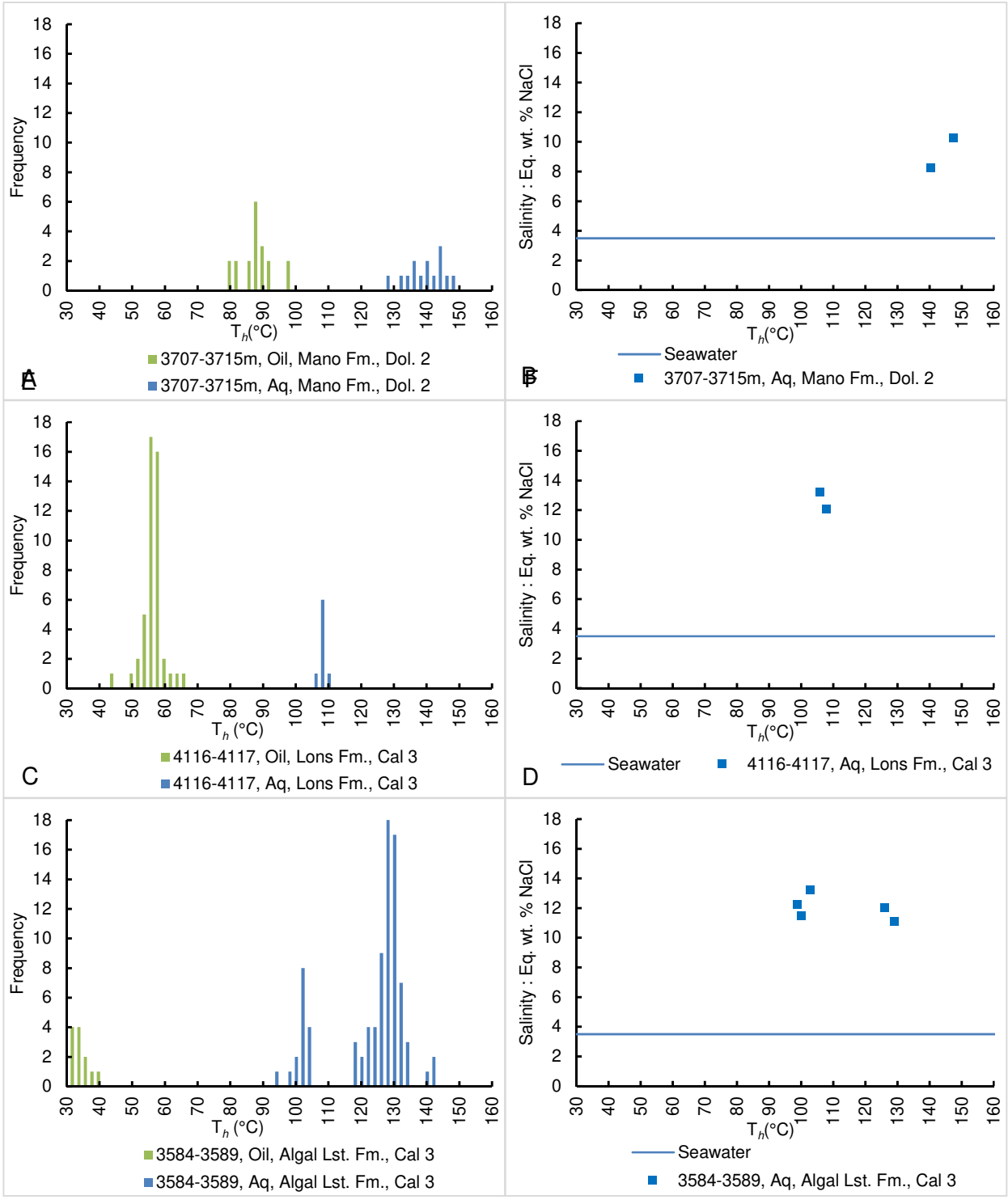

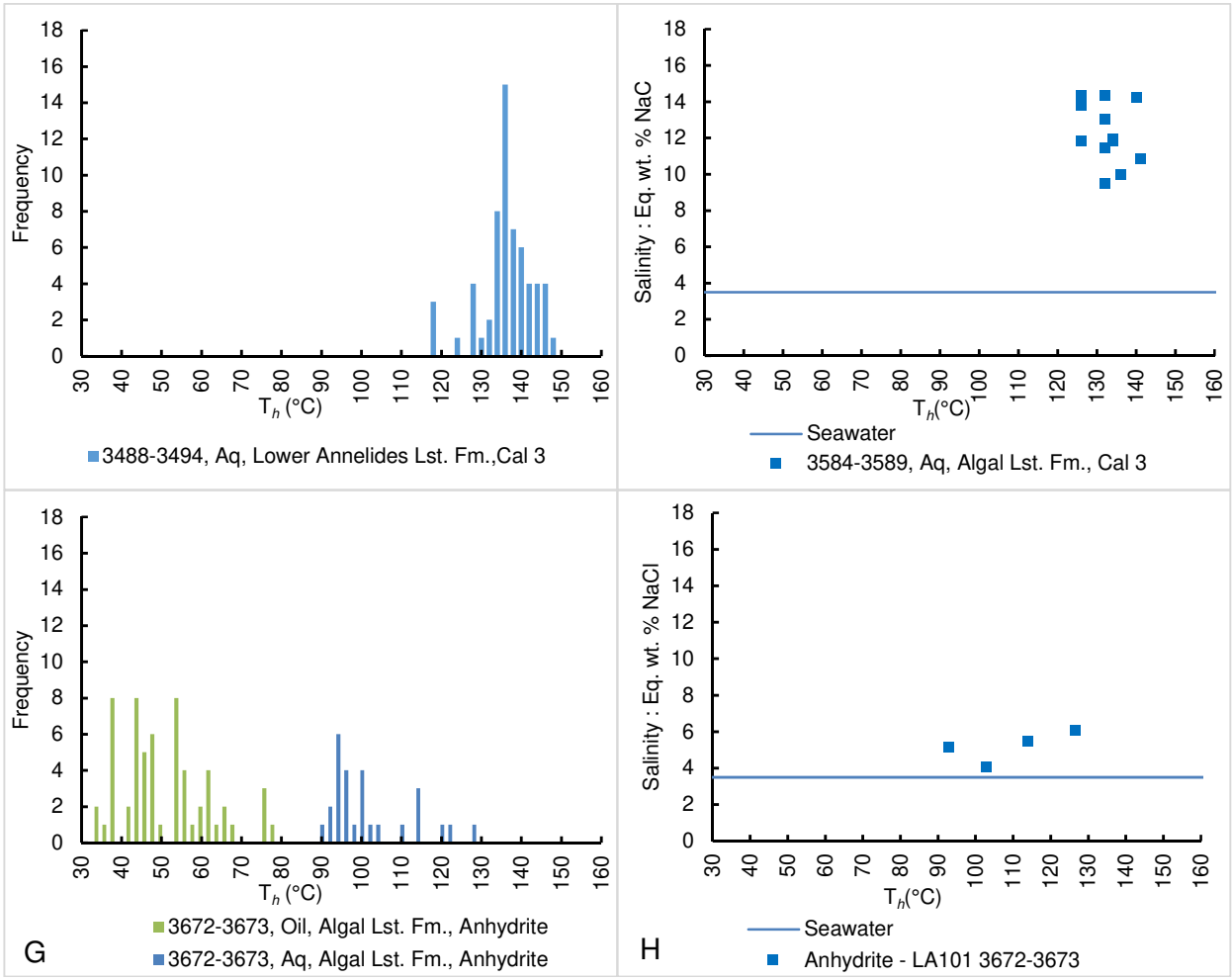

Figure 10. A: Histogram showing homogenization temperatures of aqueous and oil inclusions in the Dol.2 at a depth of 3707-3715 m in the Mano Dolomite Formation. B: T_h vs. salinity cross-plot of the studied aqueous FIs in Dol.2. C: Histogram showing homogenization temperatures of aqueous and oil inclusions in the Cal. 3 phase in the Lons formations. D: T_h vs. salinity cross-plot of the studied aqueous FIs in the Cal. 3 phase of the Lons formation. E: Histogram showing homogenization temperatures of aqueous and oil inclusions in the Cal. 3 phase in the Algal Limestone formation. F: T_h vs. salinity cross-plot of the studied aqueous FIs in the Cal. 3 phase of the Algal Limestone formation. G: Histogram showing homogenization temperatures of aqueous and oil inclusions in the Cal. 3 phase in the Annelids formation. F: T_h vs. salinity cross-plot of the studied aqueous FIs in the Cal. 3 phase of the Annelids. I: Histogram showing homogenization temperatures of aqueous and oil inclusions in the anhydrite phase at a depth of 3672-3673m in the Algal Limestone formation. K: T_h vs. salinity cross-plot of the studied aqueous FIs in the anhydrites.

The Cal. 3 sample from the Annelids formation showed only one population of two-phase aqueous inclusions with no traces of oil inclusions. This population of fluids homogenized into the liquid phase at a T_h range of 118-148°C with a mode at 136°C (Fig. 10-G). These fluids also have final ice melting temperatures between -6 and -10°C corresponding to salinity range between 9.5 and 14 wt.% NaCl (Fig. 10-H).

The studied anhydrite sample was retrieved from the Algal limestone at a depth of 3672-3673m. The primary two-phase aqueous inclusions homogenized at a T_h range of 90-128°C with the mode at 94°C (Fig. 10-I). The oil inclusions homogenized into the liquid phase at a T_h range of 32-78°C with a mode T_h at 56°C. Tm_i could not be recorded with confidence due to repetitive decrepitation

and/or darkening of the fluid inclusions. Instead, salinities were obtained from the Raman spectra of the liquid phase which indicated 4 to 6 eq. wt.% NaCl (Fig. 10-J).

All measured homogenization temperatures were repeated 3 times by cycling procedures to validate the reproducibility of the recorded T_h. The reproducibility of the all measured T_h was confined to a margin of error of no more than ±1°C, which is within the temperature increase of +2°C/min used during homogenization.

During the freezing cycle of all salinity measurements, and upon gradual heating up from -100°C, eutectic phase changes were observed at nearly -21.5°C to -22°C, a clear indication of the H_2O-NaCl fluid system (Roedder, 1990).

5.3.3 Raman Spectroscopy

Raman spectra on the liquid and gas phases of the aqueous FIs in dolomite 2, calcite 3 and anhydrite were analyzed to qualify and quantify the dissolved gases. Measurements were made at the homogenization temperatures in the liquid phase. The detected species include CH_4 and H_2S that are listed in table 2.

Table 2. Summary of the average molar fractions of H_2O, H_2S and CH_4 of the aqueous phase in the fluid inclusions. NaCl equivalent mass % were computed according to Bodnar (1993). H_2S values were determined following Jacquemet et al. (2005) while the CH_4 calculated from the Raman spectra following the outline of Caumon et al. (2014).

		Eq. mass %	Mole fractions (%)		
Aq. FIs.	T_h (°C)	NaCl	H_2O	H_2S	CH_4
SD-1	139	7.9	94.79	4.90	0.31
SD-2	140	8.24	94.41	5.34	0.25
C-1 (Lons)	107	13	97.38	2.26	0.35
C-1 (Lons)	106	12.7	97.18	2.41	0.40
C-1 (Algal)	126	12	98.06	1.71	0.23
C-2 (Algal)	129	11.1	97.45	2.35	0.19
A-1	94	5.3	98.76	0.97	0.27
A-2	96	5.1	98.81	0.85	0.34

5.3.4 Fluid Modeling

Aqueous and oil inclusions present as pairs in the same assemblage in a mineral can be tested for AIT-PIT modeling. For this purpose, pairs of aqueous and oil inclusions were selected from Dol. 2, Cal.3 and Anhydrite cement phases whose isochores are plotted in figure 11. The calculation steps are highlighted in section 3.6. As seen in figure 11, the addition of 20% H_2S into the composition of oil inclusions tend to suppress and lower the homogenization pressures.

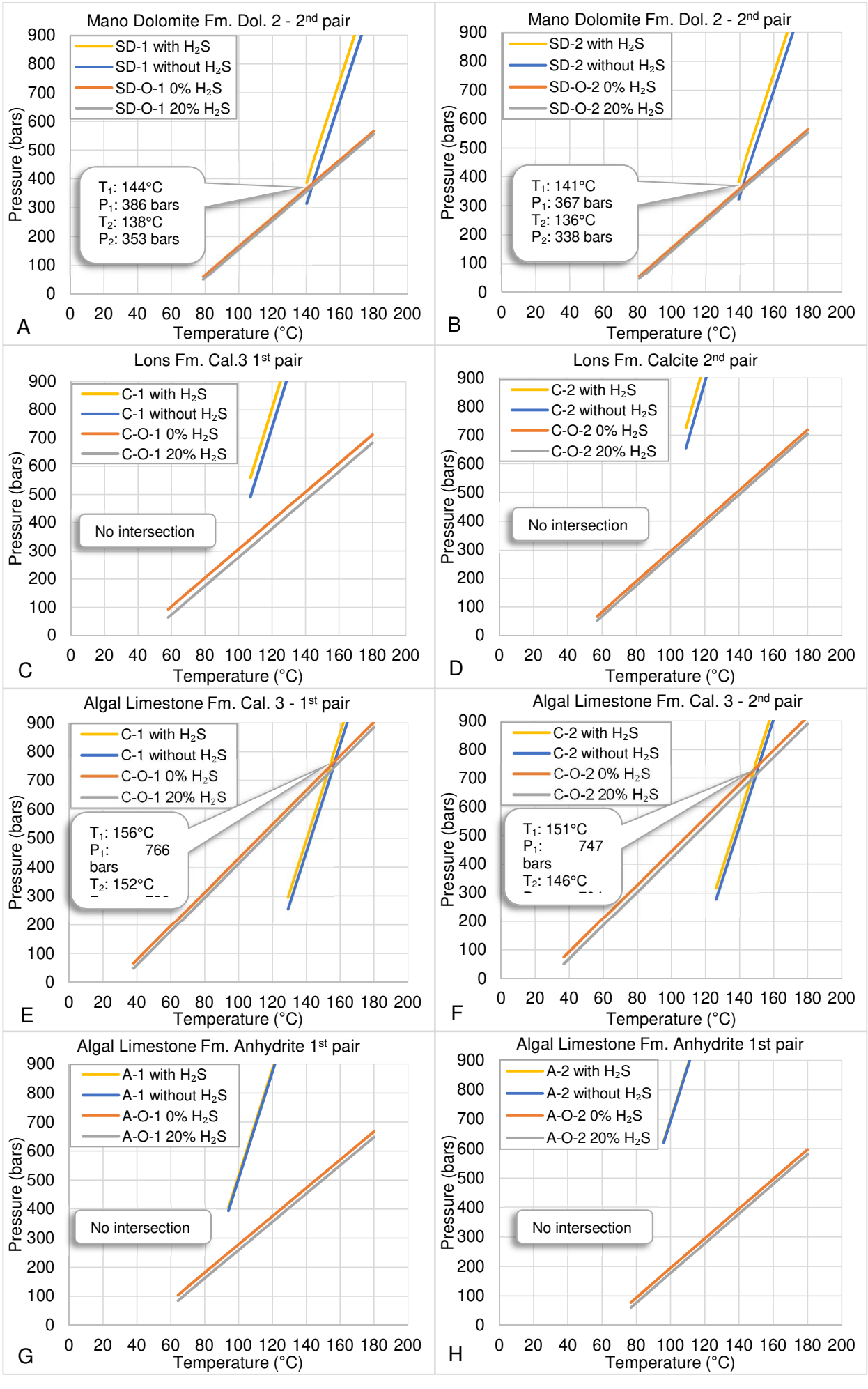
Mano Dolomite Fm. Dol. 2 - 2nd pair
SD-1 with H2S
SD-1 without H2S
SD-O-1 0% H2S
SD-O-1 20% H2S
T1: 144°C
P1: 386 bars
T2: 138°C
P2: 353 bars
Pressure (bars)
Temperature (°C)
A
Mano Dolomite Fm. Dol. 2 - 2nd pair
SD-2 with H2S
SD-2 without H2S
SD-O-2 0% H2S
SD-O-2 20% H2S
T1: 141°C
P1: 367 bars
T2: 136°C
P2: 338 bars
Pressure (bars)
Temperature (°C)
B
Lons Fm. Cal.3 1st pair
C-1 with H2S
C-1 without H2S
C-O-1 0% H2S
C-O-1 20% H2S
No intersection
Pressure (bars)
Temperature (°C)
C
Lons Fm. Calcite 2nd pair
C-2 with H2S
C-2 without H2S
C-O-2 0% H2S
C-O-2 20% H2S
No intersection
Pressure (bars)
Temperature (°C)
D
Algal Limestone Fm. Cal. 3 - 1st pair
C-1 with H2S
C-1 without H2S
C-O-1 0% H2S
C-O-1 20% H2S
T1: 156°C
P1: 766 bars
T2: 152°C
Pressure (bars)
Temperature (°C)
E
Algal Limestone Fm. Cal. 3 - 2nd pair
C-2 with H2S
C-2 without H2S
C-O-2 0% H2S
C-O-2 20% H2S
T1: 151°C
P1: 747 bars
T2: 146°C
Pressure (bars)
Temperature (°C)
F
Algal Limestone Fm. Anhydrite 1st pair
A-1 with H2S
A-1 without H2S
A-O-1 0% H2S
A-O-1 20% H2S
No intersection
Pressure (bars)
Temperature (°C)
G
Algal Limestone Fm. Anhydrite 1st pair
A-2 with H2S
A-2 without H2S
A-O-2 0% H2S
A-O-2 20% H2S
No intersection
Pressure (bars)
Temperature (°C)
H

Figure 11. Plots of the aqueous and oil inclusions isochores that are petrographically located within the same assemblages. Location of the selected fluid inclusions are found in figure 9. Plots of A and B show the isochores of aqueous and oil inclusions in the Dol. 2 of the Mano formation. C and D show the isochores of aqueous and oil inclusions of the Cal. 3 phase in the Lons formation Limestone formation. The two sets of isochores do not intersect and hence the trapping P-T conditions could not be determined. E and F represent the isochores of aqueous and oil inclusions in the Cal. 3 phase of the Algal Limestone formation. The two sets of isochores intersect and the trapping P-T conditions are noted in the bubbled boxes. G and H show the two sets of the aqueous and oil inclusions isochores of the anhydrite phase in the Algal Limestone formation, which do not intersect.

5.4 Basin Modeling

Taking into account realistic amounts of erosion that fit with the geodynamic history of the area, as well as the proper basal heat flows scenarios that fit with the previously published works (e.g. Le Marrec et al., 1995; Renard et al., 2019); the thermal basin model was calibrated as presented in figure 12. The high maturities of vitrinites were reached by increasing the basal heat flow during the Late Jurassic and Albo-Aptian rifting episodes. The amount of eroded material fit with the onlaps and toplaps geometries at the base Cretaceous, base Cenomanian and base Paleocene unconformities (Fig. 3) with 400m eroded at the top of Flysch formation, 200m at the top of the Assat marls and 50 meters at the top of the Mano Formation. During the climax of the Aptian rifting, the heat flow reached 130mW/m^2 (Renard et al., 2019). Previous works showed that this thermal peak did not cool quickly but took at least 20 to 30 Ma before decreasing again (Clerc et al., 2015; Salardon et al., 2017; Angrand et al., 2018). This was taken into account such that the peak basal heat flow reached 110 mW/m^2 at 120 Ma and took 20 Ma to decrease to 85 mW/m^2. The present-day heat flow of 45 mW/m^2 is equivalent to a geothermal gradient in Lacq close to 30°C/km (Le Marrec et al., 1995 and Renard et al., 2019).

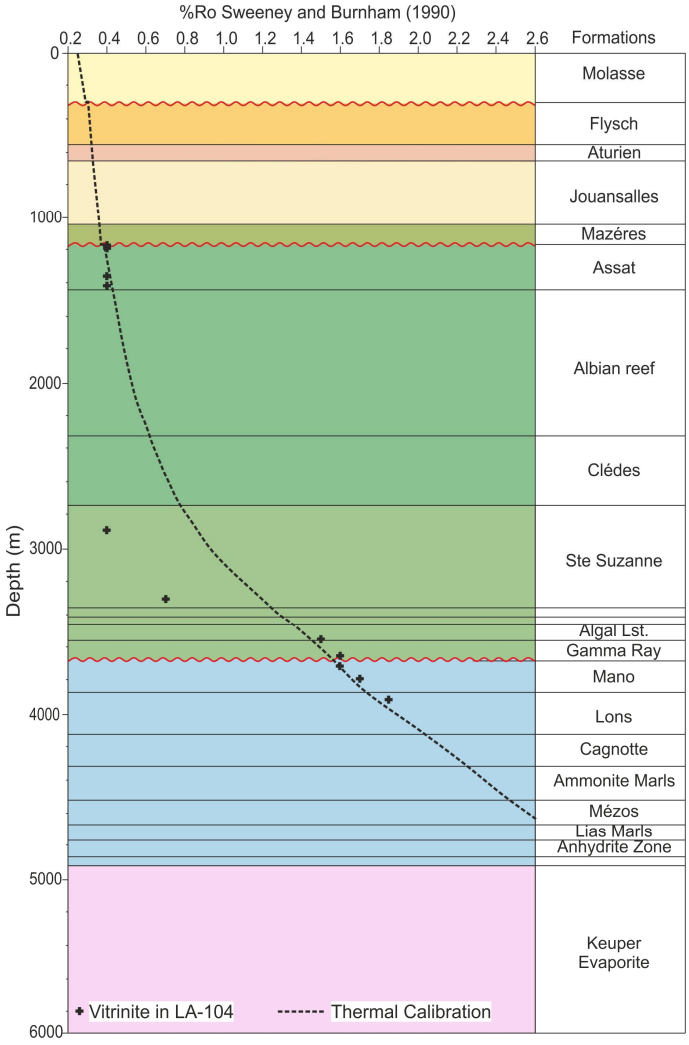

Figure 12. Thermal maturity calibration of the basin model.

6 Discussions

6.1 Fluid modeling

Figure 9 gives strong petrographic evidence of primary aqueous and oil inclusions entrapment in the studied phases. The location of fluids between growth zones or in clusters limited to individual crystals indicate a primary origin of the inclusions. Also, microthermometry results provide additional supporting evidence that can complement petrographic observations. Figure 10 shows different homogenization temperatures and salinities between the different cement phases. This difference indicates distinct fluid events, that trapped inclusions between growth zones and in clusters within individual crystals, and not as secondary fluid events that would cross-cut different cements with identical temperatures and salinities. The risk of having post-entrapment alteration and necking down was also checked. For this purpose, several lines of evidence are available to elucidate such risks or doubts. Firstly, no petrographic evidence were found to support any necking down or shape-modification of the studied fluid inclusions. There are no single-phase aqueous

603 inclusions alongside an inclusion dominated by the vapor phase, typical of a necked-down
604 inclusions. Secondly, the L/V ratio, Fv%, is consistent and stable across all studied FIs in the
605 different cement phases. Necking down or thermal resetting would result in varying Fv%. Thirdly,
606 the shape of the histogram shows a confined Gaussian distribution of frequencies without any
607 high-temperature “stretching” or thermal re-equilibration trends. The confinement of the T_h
608 measurements to limited ranges of nearly 10°-15°C variability is still a very limited range giving
609 such a diagenetic system at depths of 3.5-4 km. Finally, the good reproducibility of the
610 homogenization temperatures at room conditions, where the pressure difference is the highest
611 between the internal fluid pressure and the external atmospheric pressure, is another indication
612 that the studied cement phases are not fragile and did not undergo post-entrapment alteration.
613 Another line of evidence that supports the absence of post-entrapment alteration is the near
614 absence of decrepitation of fluid inclusions, which further supports the good reproducibility of
615 obtained T_h and the absence of post-entrapment P-T modifications. Therefore, after validating the
616 primary nature of the fluid inclusions and confirming the absence of post-entrapment alteration,
617 pairs of aqueous and oil inclusions were selected for modeling. The selection criteria focused on
618 their petrographic location between growth zones or in clusters confined to individual crystals and
619 not extending to nearby cements. The pairs of aqueous and oil inclusions were also selected to
620 represent the most common homogenization temperatures, i.e. the modes, of the FI populations.
621 Following these criteria and the modeling procedure described in the paragraph 3.6, the aqueous
622 and oil inclusions observed in the Dol. 2 phase were modeled and indicate trapping temperatures
623 of 141-144°C and pressures between 367 and 386 bars. In the case of the Cal. 3 phase, at least
624 three fluid pulses are recognized. The first fluid pulse was a mixture of aqueous and oil fluids
625 trapped contemporaneously in the calcite cement. These fluids are documented in figure 11 – E
626 and F where their isochores intersect at high-pressure conditions. The two other fluid pulses are
627 evidenced by the aqueous and oil inclusions which were not trapped simultaneously as seen in
628 figure 11 – C and D. The anhydrite phase is also a witness of multiple fluid pulses, as the
629 isochores of the aqueous and oil inclusion trapped in it do not intersect (Figure 11- G and H).
630 Modeling of trapping P-T conditions of fluid inclusions should be evaluated relative to the
631 uncertainties and limitations of the used techniques. In this study, the error range of the T_h
632 microthermometry measurements is in the order of ±1°C and for Tm_i around ±0.1°C. Quantification

errors of gases in the fluid inclusions using Raman spectroscopy should be less than 0.1 mol% as the treatment and calculation steps were repeated several times to avoid any biased baseline treatment of the Raman spectra. Finally, the processing of the 3-D image stack for the oil inclusion modeling and the quantification of the vapor volume fraction by the confocal scanning laser microscope could impose an error of no more than ±2%. Combining all these error ranges and extrapolating them to the trapping P-T estimation, a possible error range of ±15 bars and ±5°C is suspected. This uncertainty is deemed acceptable for diagenetic systems whose P-T conditions range from 100-1500 bars and 40-250°C (Pironon, 2020).

6.2 Ages of the diagenetic fluids

To obtain age constraints on the diagenetic fluids, hydrostatic and lithostatic pressures obtained from the basin model done with Petromod 1D are plotted on P-T diagram from the time the formation was deposited until present day (Fig. 13). The spike in temperature between 116 and 97 Ma refers to the high thermal anomaly associated to the Apto-Albian rifting stage. On the same figure, the trapping P-T conditions obtained from the double-isochore plots in figure 11 are also plotted. This step puts the conditions of the trapped fluids in the framework of the P-T evolution of their hosting formation and thus the timing of the trapping can be deduced. As seen in figure 13-A, the two pairs of fluid inclusions trapped in the Dol. 2 intersect the P-T domain of the Mano Dolomite formation at two age ranges: 120-116 Ma (Aptian) and 81-68 Ma (Campanian-Maastrichtian). The difference between the fluid pressure and the hydrostatic pressure amount to around 175 bars of overpressure if the 81-68 Ma age is considered. Similarly, fluids trapped in the Cal. 3 phase intersect the P-T domain of the hosting Algal Limestone formation between 109.5 and 97 Ma (Albian – Cenomanian) (Fig. 13-B). These fluids have pressures closed to the lithostatic pressure gradient, amounting to around 480 bars of overpressure relative to hydrostatic conditions. Given the petrographic evidence that clearly places the Cal. 3 phase as paragenetically younger than the saddle dolomites (Fig. 4, 6 – B and D), the Aptian age of the saddle dolomites is more realistic than the Campanian-Maastrichtian. This Aptian age is further supported by the regional dolomitization trend during the Aptian observed in the Rousse field (Renard et al., 2019) and in the Chaînons Béarnais (Motte et al., 2021; Salardon et al., 2017).

It was not possible to place an age constraint on the fluids trapped in the Anhydrite phase, because the aqueous and oil inclusions are not co-genetic and were not trapped simultaneously. Nonetheless, it is still possible to approximate their relative timing of precipitation by petrographic evidence. Figure 7-A shows a stylolite, tectonic in origin, cross-cutting an anhydrite-filled fossil-moldic pore. These tectonic stylolites were likely formed as a result of the maximum compression during the Eocene. Also, figure 7-C shows Cal.3 being partially replaced by the engulfing Anhydrite cement. Hence, the anhydrites have an age younger than the Cal. 3 phase and before the Eocene maximum compression, thus the Late Cretaceous age.

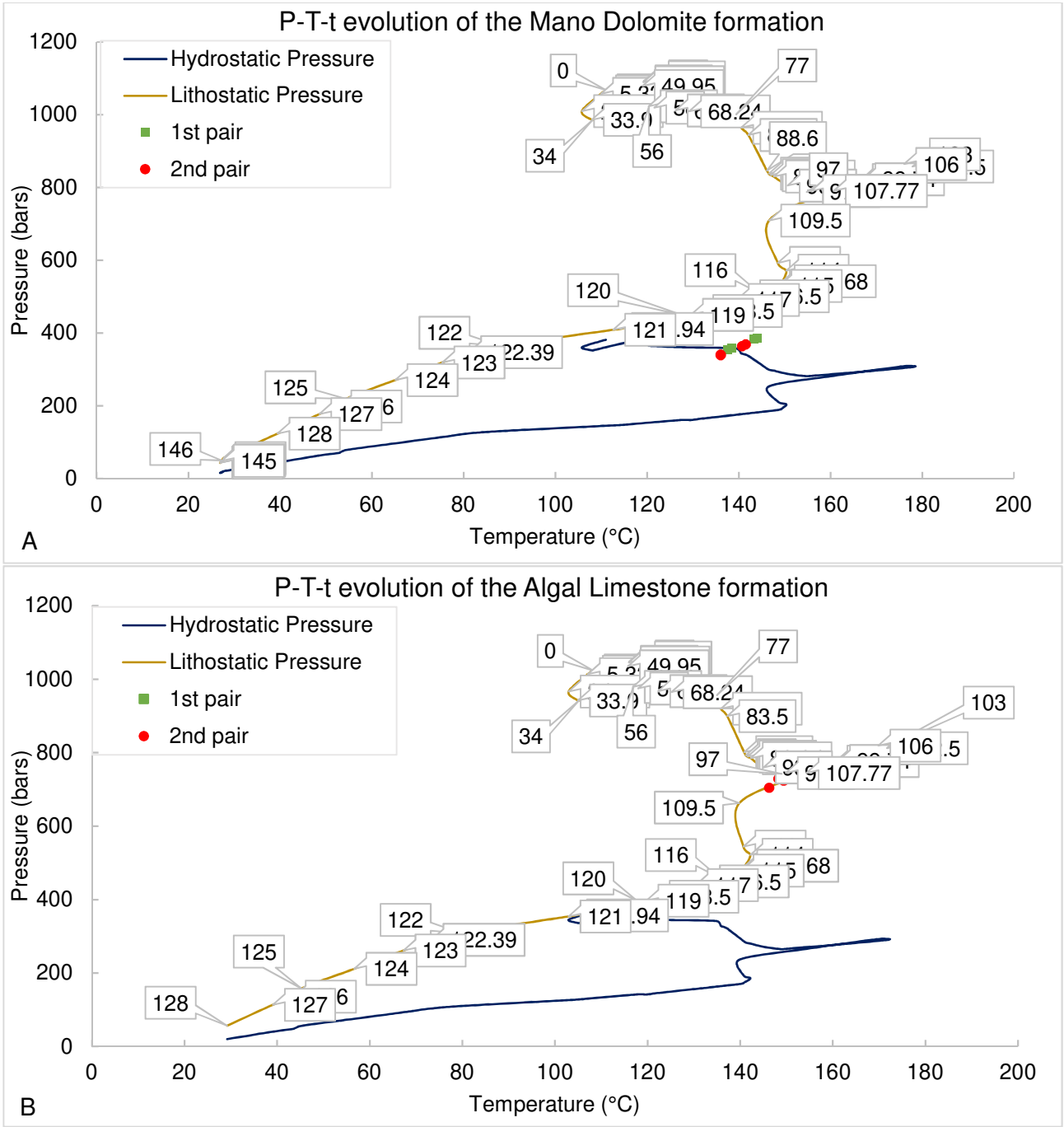

Figure 13. Evolution of the hydrostatic and lithostatic pressures deduced from Petromod 1D for the (A) Mano dolomite formation and Algal Limestone Formation (B). Number tags are ages in Ma. The green and red

points correspond to the trapping P-T conditions of the fluids determined from the intersection of the aqueous and oil inclusions isochores in figure 11.

Uncertainties about these age estimations are related mainly to the thermal model calibrated with the vitrinite data (Fig. 12). In the Mano, Algal and Lons formation, the modelled maturity is compatible with that recorded from the vitrinite data and fits well the vitrinite maturities. The misfit with the vitrinite data in the Sainte Suzanne marls is likely linked to the thermal blanket effect that these marls have, which isolated the vitrinites and prevented their higher maturities. The clays, shales and marls that constitute the Sainte Suzanne formation are characterized by significantly low thermal conductivities in the range of 0.2-1.0 $Wm^{-1}/°C$, almost half the conductivities in the surrounding media (Blackwell and Steele, 1989; Pollack and Cercone, 1994; Nunn and Lin, 2002; Clerc et al., 2015; Salardon et al., 2017).

6.3 Diagenetic model of Deep Lacq

A paragenetic sequence of diagenetic phases and events is proposed in figure 14.

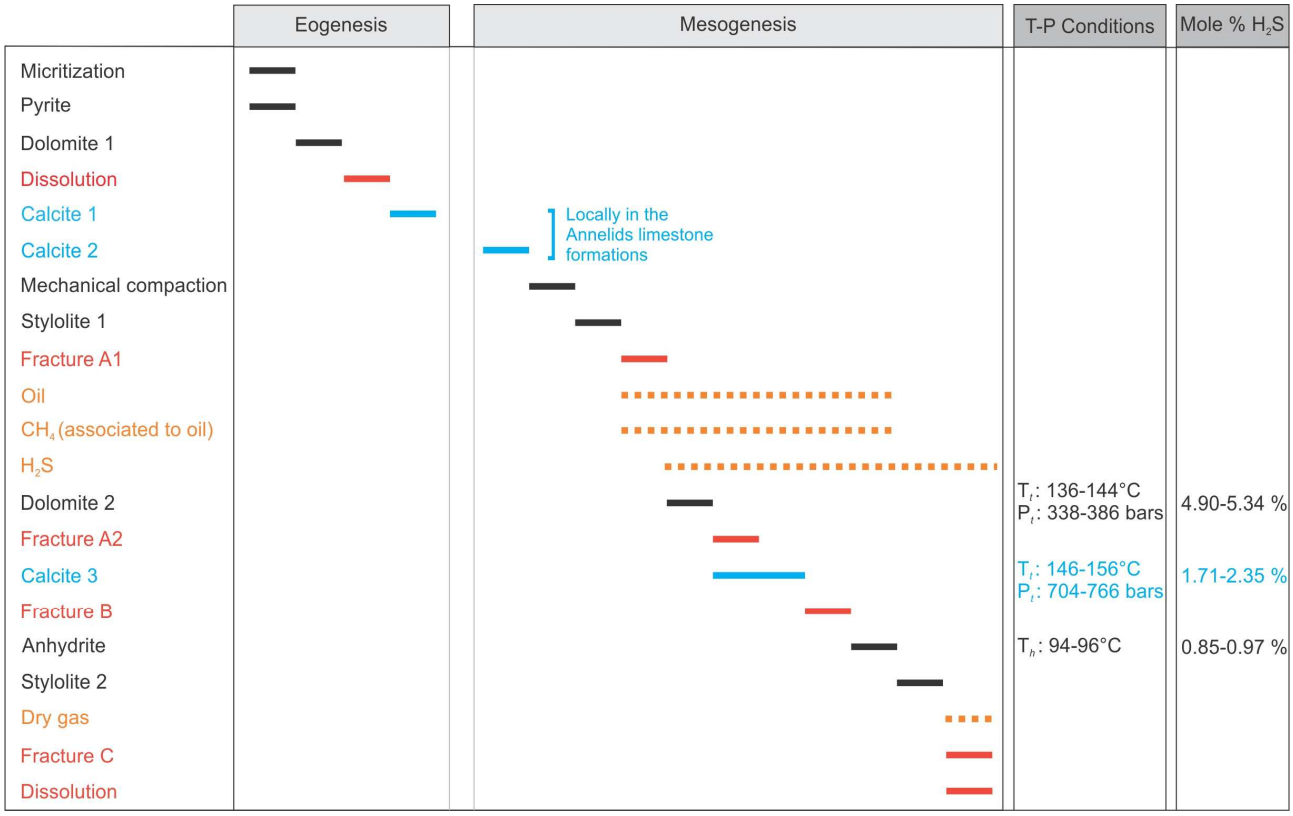

Figure 14. Paragenesis of the Lacq gas field. T_t and P_t correspond to the trapping T-P conditions respectively as deduced from fluid modeling. T_h is the homogenization temperature. The evolution of H_2S mole % is also added.

The chalky mudstone, bioclastic wackestone to packstone, as well as the pelloidal boundstone with microforaminifera, bivalves, mollusks, sponges, echinoderms and annelids are indicative of a shallow marine depositional environment, in a lagoon to reefal setting. This is also supported by

693 previous paleo-environmental reconstructions of Le Marrec et al. (1995) and Biteau et al. (2006).
694 $\delta^{18}O$ isotopes of the bulk host rocks (Fig. 8) are depleted relative to the late Jurassic seawater
695 (Veizer et al., 1999). This signature is typical of micrites which experienced crystal overgrowths at
696 higher temperatures during burial (Carpentier et al., 2014). The high-temperature impact is
697 supported by the orange CCL colors of the micritic host rocks (Figs. 4-E and 5-B,C,D) which are
698 indicative of the expected reducing conditions during burial diagenesis (Flügel, 2004). Negative
699 $\delta^{13}C$ values could be due to a possible contribution of organic matter hosted in the chalky matrix
700 (Jorgensen, 1987). Micrite rims and burrows engulfing and penetrating bioclasts (Fig. 4-A) are
701 evidences of micro-borers bacterial activity (e.g. micro-borers). The bacterial activity was
702 responsible of the precipitation of pyrite 1 phase since the framboidal clusters and their rounded to
703 anhedral shapes are typical by-products of bacterial sulfate reduction (BSR) (Machel, 2001). The
704 preferential distribution of framboidal pyrite in shells impacted by micritization is in accordance with
705 BSR, controlled by the local abundance of organic matter. Dolomite 1 is relatively early in the
706 diagenetic history (Fig. 14). It is probably the product of marine dolomitization in a shallow lagoonal
707 environment. This is partly supported by the dark core of the dolomite crystals (Fig. 4-C) and by
708 the shallow marine conditions that prevailed throughout the Jurassic and Cretaceous (Biteau et al.,
709 2006). These early dolomite phases (D1) can be considered as the analogs of the replacive
710 dolomites (RD1, RD2) that precipitated in near-surface to shallow burial environments found in the
711 Chaînons Béarnais with cretaceous ages (141-125 Ma) (Motte et al., 2021). The very small crystal
712 sizes and possible contamination with the host matrix prevented reliable collection of powders for
713 O and C isotopes analysis to further support the dolomitization model. At slightly deeper levels
714 within the meteoric eogenetic realm, local circulation in the meteoric phreatic zone, characterized
715 by fluctuations in redox conditions, precipitated the dog-tooth calcite 1 phase. The scalenohedral
716 morphology of crystals, their isopachous distribution around grains, and their zoning in CCL (Fig.
717 4-E) reflecting the fluctuations in redox states (Machel et al., 1991) support the precipitation in the
718 deep meteoric phreatic zone (Flügel, 2004; Moore, 2013). Transition to mesogenesis (Fig. 14) was
719 marked by the dominance of the reducing conditions in the calcite 2 phase with diminishing
720 influence of the percolating meteoric fluids. Calcite 1 and 2 are only observed at the level of the
721 Annelids formation and are considered as products of local pools of meteoric fluids possibly
722 supplied by the local surfaces of subaerial erosion at the Base Cretaceous unconformity (Fig. 2).

As the overburden pressure increased, mechanical compaction started and then evolved to chemical with the development of stylolites 1 (Fig. 5-A). Since the samples were collected from vertical wells that cut perpendicularly nearly horizontal strata, the orientation of the stylolite 1 planes, being nearly horizontal, allows its classification as bedding-parallel stylolites (BPS). Stylolite 1 are cross-cut by fracture A. These fractures were initially lined by dolomite 2 before being partially replaced by later calcites (Fig. 5-B). The relative $\delta^{18}O$ depletion (~-6.2‰PDB) of dolomite 2 is due to fractionation at elevated temperatures (O'Neil et al., 1969). The presence of H_2S in the aqueous inclusions (Table 2) is likely generated by Thermochemical Sulfate Reduction (TSR) as this process is well-documented in the area and is assumed to be responsible of the high H_2S concentration (up to 15% mol) of the Lacq gas field (Connan and Lacrampe-Couloume, 1993). The H_2S presence in these fluid inclusions suggests that TSR was already active when saddle dolomites precipitated. However, no evidence of *in-situ* TSR is observed here, implicating migration of TSR-derived fluids into the Deep Lacq reservoir. Saddle dolomites are mostly limited to fractures and represent a typical burial cement whose Mg source was likely the dissolution and recrystallization of the early dolomites as a result of pH lowering during the first stages of organic matter maturation (Moore, 2013). Such a scenario can justify the elevated $\delta^{18}O$ values calculated for the parent fluid of dolomite of 8.1-10.1 ‰SMOW (Fig. 15-B). The dissolution of low temperature carbonates in semi-closed conditions is an efficient way to enrich the $\delta^{18}O$ of parent fluids and provide a suitable Mg source. The partially dissolved and recrystallized early dolomites, with their corroded rims and/or cores (Fig. 4-C) provide direct evidence of this Mg source.

The high salinities and enriched $\delta^{18}O$ values for the dolomite-forming fluids, indicate a mixture between the Triassic evaporites at the core of the Lacq anticline (Fig. 3) and the recrystallization of earlier dolomites during the Aptian hyperextension. Mg derived from a marine source influenced by high-temperature serpentization reactions (Scribano et al., 2017) could also be possible given the geodynamic context that was impacted by the thermal anomaly during the Aptian hyperextension. This dolomite phase (Dol. 2) is similarly documented by Motte et al. (2021) as phases DC2, DC3 and DC4 in the Chaînons Béarnais, and as Dol 2 and Dol 3 by Renard et al. (2019) in the Rousse field.

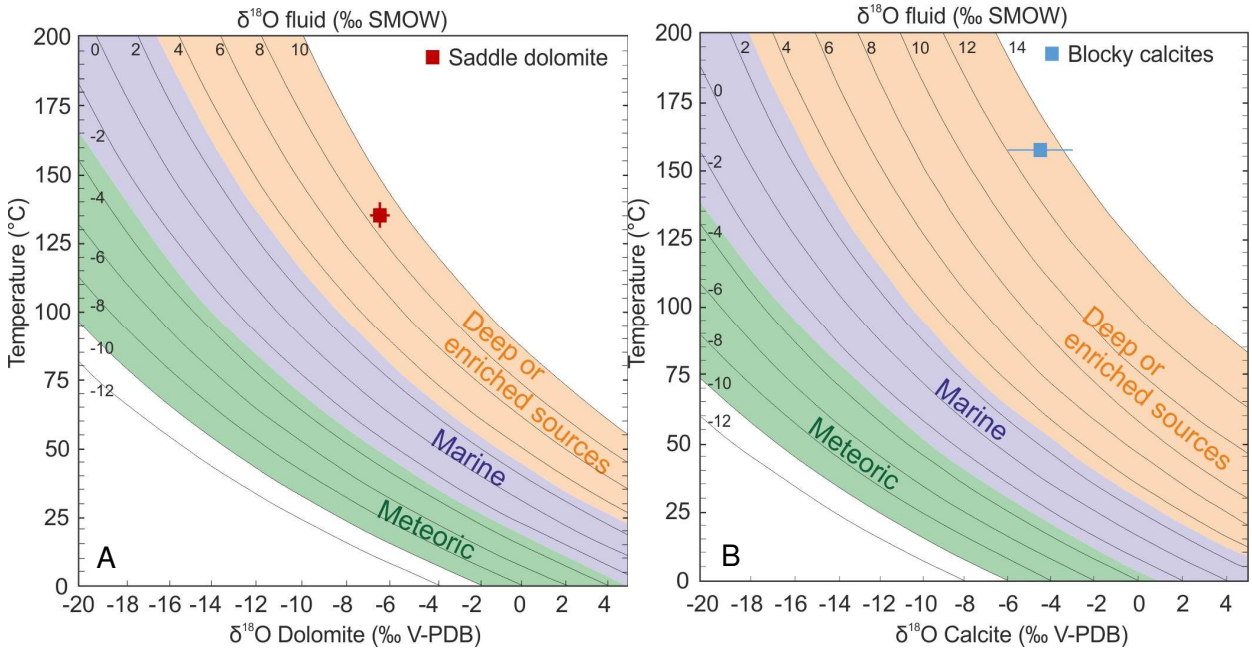

Figure 15. Fractionation curves of Horita (2014) to determine the $\delta^{18}O$ (SMOW) values of the parent fluids that precipitated the saddle dolomite phase.

Oil has likely migrated to the Deep Lacq reservoir during the precipitation of Dol. 2 as suggested by the primary oil inclusions. Source rock maturity modeling indicate that the entrance to the oil windows, with vitrinite reflectance of ~0.6% PRv (oil) has occurred during the Lower Cretaceous on the crest and the NE limb of the Lacq structure (Sejourné, 1995). Such a model can explain the coeval entrapment of oil and aqueous inclusions in Dol. 2 and is in accordance with the timing suggested in figure 13-A.

The Albian-Cenomanian age of the calcites correspond to a phase of post-rift uplift and thermal re-equilibration (Masini et al., 2014; Ford et al., 2016). This change in tectonic activity triggered a new fracturing event (A2) that reopened fracture set A1 (Fig. 5-B) and allowed Ca-rich fluids to circulate. The dull orange to yellow luminescence suggests a precipitation under reducing conditions (Machel, 1985). The depletion in $\delta^{18}O$ (-2.8 and -5.63‰PDB) (Fig. 8) is also due to fractionation at elevated temperatures (Horita, 2014). The $\delta^{13}C$ of the Cal.3 is in the same domain as that of the Dol. 2 and represents typical signatures of burial cements whose fluids have been buffered by the surrounding media (Moore, 2013). The $\delta^{18}O$ of the parent fluids that precipitated the calcite 3 is enriched and reach +8.7 ‰ SMOW (Fig. 15-A). This enrichment is indicative of a contribution of a deep source of fluids. The most likely scenario is the depletion of Mg in the Triassic brine that have precipitated the saddle dolomites leaving behind fluids enriched in $\delta^{18}O$, depleted in Mg and relatively saturated in Ca. The similar salinities between the fluids trapped in

772 the saddle dolomites and the Cal. 3 (Fig. 10 – B, D, F and H) provide strong evidence to the
773 continued leaching of the Triassic saline source, but with the cessation of supply of mantellic Mg
774 during this phase.

775 After calcite cementation, the massive anhydrites precipitated along the fracture set C. Multiple
776 sulfur isotopes values in this anhydrite phase ($\delta^{34}S$ between 18.97 and 19.12‰ and $\Delta^{33}S$ between
777 0.017 and 0.023‰) are consistent with the overall Keuper seawater signature recorded in CAS at
778 $\delta^{34}S$ = 20.6‰ ±5.4 and $\Delta^{33}S$ = 0.000‰ ±0.025 (Wu et al., 2010 – 2014). This further supports a
779 direct link between Deep Lacq and the underlying Triassic evaporites at the core of the Lacq
780 Anticline (Fig. 3). The structural link between the Triassic core and the Jurassic reservoirs of Deep
781 Lacq was made possible through the major thrust fault that separates the Southern Lacq Basin
782 from the Lacq Anticline, as well as the extensional fractures on top of the Triassic core that cut
783 through the Jurassic formations (Fig. 3). The precipitation of anhydrites has most likely occurred
784 during the onset of the N-S compression which allowed the upward circulation of dissolved sulfates
785 by pressure gradients within the anticline, before being intercepted by the impermeable formation
786 of the Sainte Suzanne Marls. This circulation scheme explains the massive precipitation of
787 anhydrite just a few meters below this formation (Fig. 6-A).

788 The infilling and supply of gases to the Deep Lacq reservoir was likely a gradual process and not a
789 sudden pulse. This is witnessed by the fact that dissolved gases were trapped in the fluid
790 inclusions of the Dol.2, Cal. 3 and anhydrite phases (table 2). Basin modeling done in this work,
791 supported by Sejourné (1995), indicates an entrance to oil window and, shortly afterwards the gas
792 window, during the Aptian thermal anomaly associated to the hyperextension event. The H_2S
793 quantity was highest in the Aptian Dol. 2 and decreased gradually to the Paleogene anhydrites.
794 The difference in timing between fluid circulation, mineral precipitation and gas charging is the
795 reason for the absence of gas inclusions in the studied phases. Basin modeling done in this work
796 and supported by Michels et al. (2021) confirm the rapid maturity of organic matter and cracking
797 from oil to gas since the Cretaceous hyperextension, but it is only recently, during the Paleogene
798 compression, that the main gas infilling of the reservoir occurred. This is mainly due to the lack of
799 pathways between the source and reservoirs rocks, which was later made possible via the fracture
800 network formed during the Paleogene orogeny (Fig. 16). The fact that no secondary gas inclusions

were observed is supported by the fact that the petroleum system entered into the dry gas window without any aqueous phase to aid in the fracture-healing processes and fluid entrapment

An illustrative summary of the main geodynamic events and associated diagenetic modifications is compiled in figure 16.

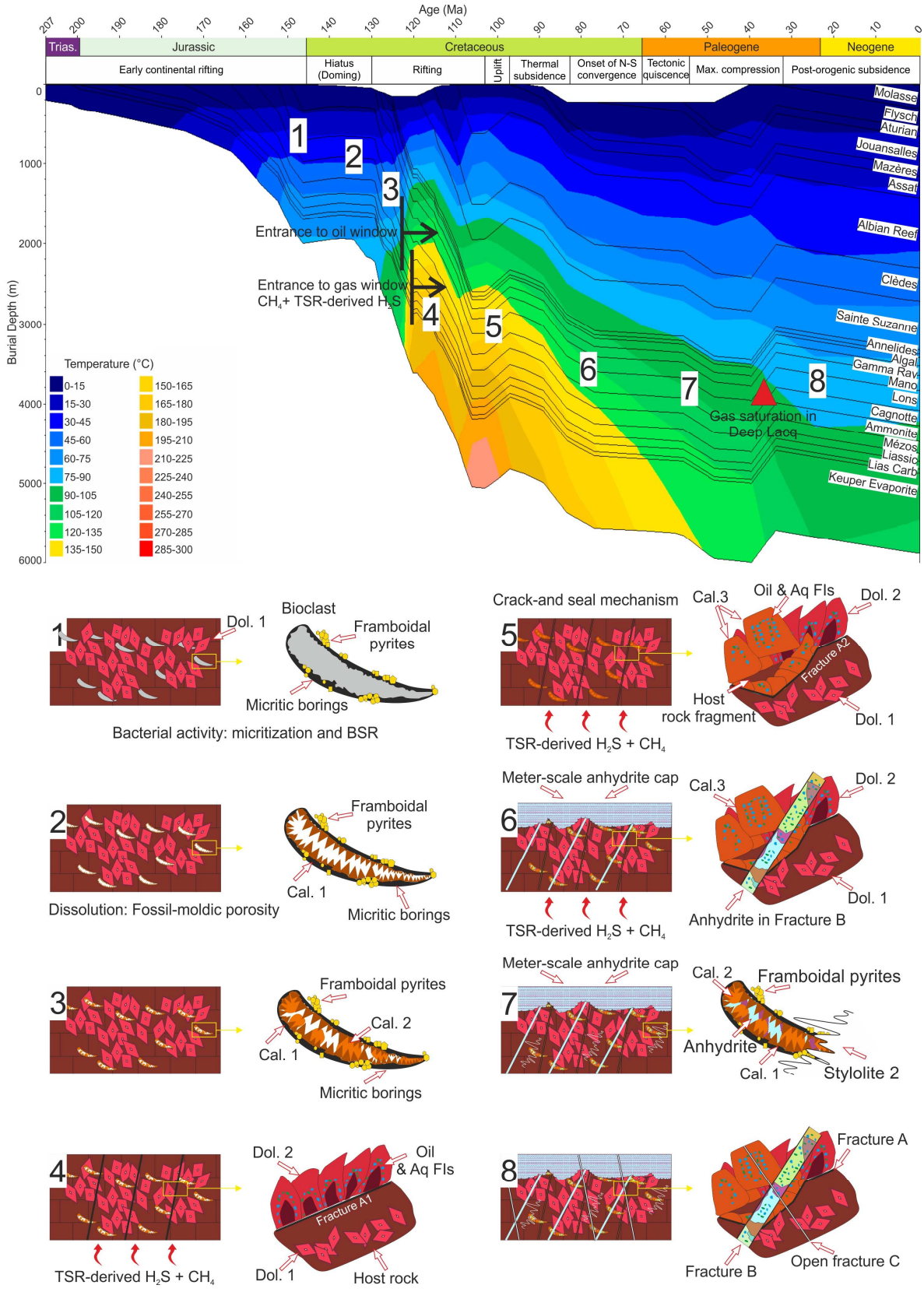

Figure 16. Summary of the main geodynamic, diagenetic and fluid events relative to the burial history of Deep Lacq. Colors of the schematic diagrams are based on the CCL petrography.

7 Conclusions

This work highlights the power of applying a multi-modeling approach to reveal the diagenetic history in a complex geodynamic setting. After a detailed petrographic analysis of all the phases present, the multitude of equations of states used in AIT-PIT modeling provided valuable insight into the fluids P-T conditions. These in turn were then validated against the basin history to place age constraints on the timing of fluids circulation.

The diagenesis of the giant Deep Lacq reservoir has been dependent on a geological heritage with two main events: a rifting phase and a convergence phase. Before these two major events, diagenesis was insignificant and limited mostly to bacterial activity as revealed by micritization and BSR-related framboidal pyrites.

The Aptian rifting and hyperextension enabled the circulation of hot deeply sourced fluids enriched in Mg, which triggered a limited event of fracture-related hydrothermal dolomitization. Fractures connected Deep Lacq to the Triassic salt core, which provided Mg^{2+} and NaCl to precipitate the saddle dolomites (Dol. 2). Additional Mg for dolomitization was provided by the dissolution and recrystallization of early dolomites. The connection to a serpentine-related source of fluids remains a likely scenario given the geodynamic context and the mantle exhumation event during the Aptian hyperextension. At the same time, the source rock entered the oil window and shortly afterwards the gas window, TSR started and gas and oil started to migrate. The most likely kitchen for TSR reactions is the deeper South Lacq Basin and not *in-situ* within the Lacq field as no evidence of local TSR were recognized in all the studied samples.

Continued fracturing events resulted in the entrapment of multiple populations of aqueous and oil inclusions in the Cal. 3 phase. This phase is a major pore-reducing cement that precipitated during Albian to Cenomanian, at the time when the basin experienced post-rift doming and thermal relaxation.

With the onset of the Pyrenean orogeny and the associated structural reconfiguration, new pathways and fractures introduced sulphate-rich fluids that precipitated anhydrite cements. The upper age limit was constrained by the Eocene compression tectonic stylolites that crosscut the anhydrites. During the Pyrenean orogeny, the gas reservoirs of Deep Lacq have likely reached their saturation capacity of dry gas that prevented further diagenetic cements to precipitate.

In this Jurassic reservoir, the number of diagenetic events appears to be less than in the "Chaînons Béarnais", a well-known zone where the absence of hydrocarbon trapping favors a longer recording of the diagenetic history.

The multitude of analytical approaches used in this research opens new perspectives to unravel the infilling and preservation history of petroleum reservoirs. Several basins have undergone a complex diagenetic history due to their geodynamic context during a complete or incomplete Wilson cycle. The combination of techniques used here is a key to deciphering the real timing, fluid composition and P-T path of fluid circulations in such complex areas.

8 Acknowledgments

This work was funded by TOTAL EP-R&D and the Center de Recherches sur la Géologie des Matières Premières Minérales et Energétiques (CREGU), contract number FR00008500 - CREGU/T25. Sylvain Calassou and the colleagues from the Center Scientifique et Technique Jean Féger de TOTAL (CSTJF-TOTAL) are warmly thanked for providing access to their facilities and data archives to conduct this research. Olivier Fonta from GEOPETROL is thanked for providing access to the core samples. Pierre Cartigny from the Institut de Physique du Globe de Paris (IPGP) is also acknowledged for his assistance with the multiple sulfur isotopes analysis. The authors also thank Silvia Lasala from the School of Chemical Industry (ENSIC) - Laboratoire Réactions et Génie des Procédés (LRPG) in Nancy for her assistance in calculating the composition of the fluid inclusions. The authors are grateful to the constructive comments of the reviewer that have improved the quality of the manuscript.

9 References

Angrand, P., Ford, M., Watts, A.B., 2018. Lateral Variations in Foreland Flexure of a Rifted Continental Margin: The Aquitaine Basin (SW France). Tectonics 37, 430–449. https://doi.org/10.1002/2017TC004670

Biteau, J., Le Marrec, A., Le Vot, M., Masset, J.-M., 2006. The Aquitaine Basin. Pet. Geosci. 12, 247–273. https://doi.org/10.1144/1354-079305-674

Blackwell, D.D., Steele, J.L., 1989. Thermal conductivity of sedimentary rocks: measurement and significance, in: Thermal History of Sedimentary Basins. Springer, New York, pp. 13–36.

865 Bodnar, R.J., 1993. Revised equation and table for determining the freezing point depression of
866 H2O-Nacl solutions. Geochim. Cosmochim. Acta 57, 683–684. https://doi.org/10.1016/0016-
867 7037(93)90378-A

868 Bourdet, J., Pironon, J., Levresse, G., Tritlla, J., 2010. Petroleum accumulation and leakage in a
869 deeply buried carbonate reservoir, Níspero field (Mexico). Mar. Pet. Geol. 27, 126–142.
870 https://doi.org/10.1016/j.marpetgeo.2009.07.003

871 Bourdet, J., Pironon, J., Levresse, G., Tritlla, J., 2008. Petroleum type determination through
872 homogenization temperature and vapour volume fraction measurements in fluid inclusions.
873 Geofluids 8, 46–59. https://doi.org/10.1111/j.1468-8123.2007.00204.x

874 Carpentier, C., Brigaud, B., Blaise, T., Vincent, B., Durlet, C., Boulvais, P., Pagel, M., Hibsch, C.,
875 Yven, B., Lach, P., Cathelineau, M., Boiron, M., Landrein, P., Buschaert, S., 2014. Impact of
876 basin burial and exhumation on Jurassic carbonates diagenesis on both sides of a thick clay
877 barrier (Paris Basin, NE France). Mar. Pet. Geol. 53, 44–70.
878 https://doi.org/10.1016/j.marpetgeo.2014.01.011

879 Caumon, M.-C., Tarantola, A., Mosser-Ruck, R., 2015. Raman spectra of water in fluid inclusions:
880 I. Effect of host mineral birefringence on salinity measurement. J. Raman Spectrosc. 46, 969–
881 976. https://doi.org/10.1002/jrs.4708

882 Caumon, M.C., Robert, P., Laverret, E., Tarantola, A., Randi, A., Pironon, J., Dubessy, J., Girard,
883 J.P., 2014. Determination of methane content in NaCl-H2O fluid inclusions by Raman
884 spectroscopy. Calibration and application to the external part of the Central Alps
885 (Switzerland). Chem. Geol. 378–379, 52–61. https://doi.org/10.1016/j.chemgeo.2014.03.016

886 Clerc, C., Lagabrielle, Y., 2014. Thermal control on the modes of crustal thinning leading to mantle
887 exhumation: Insights from the Cretaceous Pyrenean hot paleomargins. Tectonics 33, 1340–
888 1359. https://doi.org/10.1002/2013TC003471

889 Clerc, C., Lahfid, A., Monié, P., Lagabrielle, Y., Chopin, C., Poujol, M., Boulvais, P., Ringenbach,
890 J.-C., Masini, E., de St Blanquat, M., 2015. High-temperature metamorphism during extreme
891 thinning of the continental crust: a reappraisal of the North Pyrenean passive paleomargin.
892 Solid Earth 6, 643–668. https://doi.org/10.5194/se-6-643-2015

893 Connan, J., Lacrampe-Couloume, G., 1993. The Origin of the Lacq Superieur Heavy Oil
894 Accumulation and of the Giant Lacq Inferieur Gas Field (Aquitaine Basin, SW France), in:
895 Bordenave, M.L. (Ed.), Applied Petroleum Geochemistry. Editions Technip, Paris, pp. 464–
896 488.

897 Corre, B., Lagabrielle, Y., Labaume, P., Fourcade, S., Clerc, C., Ballèvre, M., 2016. Deformation
898 associated with mantle exhumation in a distal, hot passive margin environment: New
899 constraints from the Saraillé Massif (Chaînons Béarnais, North-Pyrenean Zone). Comptes
900 Rendus Geosci. 348, 279–289. https://doi.org/10.1016/j.crte.2015.11.007

901 Curnelle, R., Dubois, P., 1986. Evolution mesozoique des grands bassins sedimentaires français;
902 bassins de Paris, d'Aquitaine et du Sud-Est. Bull. la Société Géologique Fr. 8, 529–546.

903 Diamond, L.W., Tarantola, A., 2015. Interpretation of fluid inclusions in quartz deformed by weak
904 ductile shearing: Reconstruction of differential stress magnitudes and pre-deformation fluid
905 properties. Earth Planet. Sci. Lett. 417, 107–119. https://doi.org/10.1016/j.epsl.2015.02.019

906 Duan, Z., Mao, S., 2006. A thermodynamic model for calculating methane solubility, density and
907 gas phase composition of methane-bearing aqueous fluids from 273 to 523K and from 1 to
908 2000bar. Geochim. Cosmochim. Acta 70, 3369–3386.
909 https://doi.org/10.1016/j.gca.2006.03.018

910 Duan, Z., Møller, N., Weare, J.H., 1996. A general equation of state for supercritical fluid mixtures
911 and molecular dynamics simulation of mixture PVTX properties. Geochim. Cosmochim. Acta
912 60, 1209–1216. https://doi.org/10.1016/0016-7037(96)00004-X

913 Duan, Z., Møller, N., Weare, J.H., 1992a. Molecular dynamics simulation of PVT properties of
914 geological fluids and a general equation of state of nonpolar and weakly polar gases up to
915 2000 K and 20,000 bar. Geochim. Cosmochim. Acta 56, 3839–3845.
916 https://doi.org/10.1016/0016-7037(92)90175-I

917 Duan, Z., Møller, N., Weare, J.H., 1992b. An equation of state for the CH4-CO2-H2O systems: II.
918 mixtures from 50 to 1000°C and 0 to 1000 bar. Geochim. Cosmochim. Acta 59, 1533–1538.

919 Elias Bahnan, A., Carpentier, C., Pironon, J., Ford, M., Ducoux, M., Barré, G., Mangenot, X.,
920 Gaucher, E.C., 2020. Impact of geodynamics on fluid circulation and diagenesis of carbonate

921 reservoirs in a foreland basin: Example of the Upper Lacq reservoir (Aquitaine basin, SW
922 France). Mar. Pet. Geol. 111, 676–694. https://doi.org/10.1016/j.marpetgeo.2019.08.047

923 Flügel, E., 2004. Microfacies of Carbonate Rocks. Springer Berlin Heidelberg, Berlin, Heidelberg.
924 https://doi.org/10.1007/978-3-662-08726-8

925 Ford, M., Hemmer, L., Vacherat, A., Gallagher, K., Christophoul, F., 2016. Retro-wedge foreland
926 basin evolution along the ECORS line, eastern Pyrenees, France. J. Geol. Soc. London. 173,
927 419–437. https://doi.org/10.1144/jgs2015-129

928 Fréchengues, M., Martini, R., Peybernès, B., Zaninetti, L., 1990. Mise en évidence d'associations
929 de Foraminifères benthiques dans la séquence de dépôt ladino-?carnienne du «Muschelkalk»
930 des Pyrénées Catalanes (France, Espagne). Zaninetti, Louisette Publ. Comptes rendus
931 l'Academie des Sci. II, Mécanique, Phys. Chim. Sci. l'univers, Sci. la terre. 310, 667–673.

932 Horita, J., 2014. Oxygen and carbon isotope fractionation in the system dolomite–water–CO2 to
933 elevated temperatures. Geochim. Cosmochim. Acta 129, 111–124.
934 https://doi.org/10.1016/j.gca.2013.12.027

935 Hulston, J.R., Thode, H.G., 1965. Variations in the S 33 , S 34 , and S 36 contents of meteorites
936 and their relation to chemical and nuclear effects. J. Geophys. Res. 70, 3475–3484.
937 https://doi.org/10.1029/JZ070i014p03475

938 Incerpi, N., Manatschal, G., Martire, L., Bernasconi, S.M., Gerdes, A., Bertok, C., 2020.
939 Characteristics and timing of hydrothermal fluid circulation in the fossil Pyrenean
940 hyperextended rift system: new constraints from the Chaînons Béarnais (W Pyrenees). Int. J.
941 Earth Sci. 109, 1071–1093. https://doi.org/10.1007/s00531-020-01852-6

942 Jacquemet, N., Pironon, J., 2006. Durabilité des matériaux de puits pétroliers dans le cadre d'une
943 séquestration géologique de dioxyde de carbone et d'hydrogène sulfuré. Université Henri
944 Poincaré Nancy-I.

945 Jacquemet, N., Pironon, J., Caroli, E., 2005. New Experimental Procedure for Simulation of H2S +
946 CO2 Geological Storage. Application to Well Cement Aging. Oil Gas Sci. Technol. – Rev. IFP
947 60, 193–206.

948 Jammes, S., Lavier, L., Manatschal, G., 2010. Extreme crustal thinning in the Bay of Biscay and

949 the Western Pyrenees: From observations to modeling. Geochemistry, Geophys. Geosystems
950 11, n/a-n/a. https://doi.org/10.1029/2010GC003218

951 Jammes, S., Manatschal, G., Lavier, L., Masini, E., 2009. Tectonosedimentary evolution related to
952 extreme crustal thinning ahead of a propagating ocean: Example of the western Pyrenees.
953 Tectonics 28, n/a-n/a. https://doi.org/10.1029/2008TC002406

954 Jorgensen, N.O., 1987. Oxygen and carbon isotope compositions of Upper Cretaceous chalk from
955 the Danish sub-basin and the North Sea Central Graben. Sedimentology 34, 559–570.
956 https://doi.org/10.1111/j.1365-3091.1987.tb00786.x

957 Kitayama, Y., Thomassot, E., Galy, A., Golovin, A., Korsakov, A., D'Eyrames, E., Assayag, N.,
958 Bouden, N., Ionov, D., 2017. Co-magmatic sulfides and sulfates in the Udachnaya-East pipe
959 (Siberia): A record of the redox state and isotopic composition of sulfur in kimberlites and their
960 mantle sources. Chem. Geol. 455, 315–330. https://doi.org/10.1016/j.chemgeo.2016.10.037

961 Le-Marrec, A., D'Aboville, O., Delahaye, S., Lagarigue, J., Moen Maurel, L., Dore, M., Lang, J.,
962 1995. Synthèse Géodynamique du Bassin d'Arzacq et de ses bordures. Elf Aquitaine Prod.
963 95, 43.

964 Le-vot, M., Biteau, J.J., Masset, J.M., 1996. The Aquitaine Basin: Oil and gas production in the
965 foreland of the Pyrenean fold-and-thrust belt. New exploration perspectives. Peri-Tethys
966 Mem. 2 170, 159–171.

967 Lucas, C., 1985. Le grès rouge du versant nord des Pyrénées: essai sur la géodynamique de
968 dépôts continentaux du Permien et du Trias. Univ. Toulouse.

969 Machel, H.., 2001. Bacterial and thermochemical sulfate reduction in diagenetic settings — old and
970 new insights. Sediment. Geol. 140, 143–175. https://doi.org/10.1016/S0037-0738(00)00176-7

971 Machel, H.G., 1985. Cathodoluminscence in Calcite and Dolomite and Its Chemical Interpretation.
972 Geosci. Canada 12, 139–147.

973 Machel, H.G., Buschkuehle, B.E., 2008. Diagenesis of the Devonian Southesk-Cairn Carbonate
974 Complex, Alberta, Canada: Marine Cementation, Burial Dolomitization, Thermochemical
975 Sulfate Reduction, Anhydritization, and Squeegee Fluid Flow. J. Sediment. Res. 78, 366–389.
976 https://doi.org/10.2110/jsr.2008.037

977 Machel, H.G., Mason, R., Mariano, A., Mucci, A., 1991. Causes and emission of luminescence in
978 calcite and dolomite, in: Barker, C.E., Burruss, R.C., Kopp, O.C., Machel, H.G., Marshall, D.J.,
979 Wright, P., Colbum, H.Y. (Eds.), Luminescence Microscopy and Spectroscopy: Qualitative
980 and Quantitative Applications. SEPM (Society for Sedimentary Geology), pp. 9–25.
981 https://doi.org/10.2110/scn.91.25

982 Mankiewicz, P.J., Pottorf, R.J., Kozar, M.G., Vrolijk, P., 2009. Gas geochemistry of the Mobile Bay
983 Jurassic Norphlet Formation: Thermal controls and implications for reservoir connectivity. Am.
984 Assoc. Pet. Geol. Bull. 93, 1319–1346. https://doi.org/10.1306/05220908171

985 Masini, E., Manatschal, G., Tugend, J., Mohn, G., Flament, J.-M., 2014. The tectono-sedimentary
986 evolution of a hyper-extended rift basin: the example of the Arzacq–Mauléon rift system
987 (Western Pyrenees, SW France). Int. J. Earth Sci. 103, 1569–1596.
988 https://doi.org/10.1007/s00531-014-1023-8

989 Michels, R., Gaucher, E.C., Pironon, J., Elias Bahnan, A., Rallakis, D., Barré, G., Calassou, S.,
990 2021. Fluids evolutions from rift to post-orogenic stages: example of the Northern Pyrenees
991 (France), in: Bali, E. (Ed.), European Current Research on Fluid and Melt Inclusions.
992 University of Iceland, p. 82.

993 Moore, C.H., 2013. Carbonate Reservoirs, 2nd ed. ed. Elsevier, Amsterdam.

994 Motte, G., Hoareau, G., Callot, J.-P., Révillon, S., Piccoli, F., Calassou, S., Gaucher, E.C., 2021.
995 Rift and salt-related multi-phase dolomitization: example from the northwestern Pyrenees.
996 Mar. Pet. Geol. 126, 104932. https://doi.org/10.1016/j.marpetgeo.2021.104932

997 Nader, F.H., 2003. Petrografische en geochemische studie van de Kesrouane Formatie (Jura),
998 Mount Libanon : implicaties met betrekking tot dolomitisatie en petroleum geologie. Katholieke
999 Universiteit Leuven (Afd. Fysicochemische Geologie) and the Lebanese National Council for
1000 Scientific Research.

1001 Nunn, J.A., Lin, G., 2002. Insulating effect of coals and organic rich shales: implications for
1002 topography-driven fluid flow, heat transport, and genesis of ore deposits in the Arkoma Basin
1003 and Ozark Plateau. Basin Res. 14, 129–145. https://doi.org/10.1046/j.1365-
1004 2117.2002.00172.x

1005 O'Neil, J.R., Clayton, R.N., Mayeda, T.K., 1969. Oxygen Isotope Fractionation in Divalent Metal
1006 Carbonates. J. Chem. Phys. 51, 5547–5558. https://doi.org/10.1063/1.1671982

1007 Pearce, N.J.G., Perkins, W.T., Westgate, J.A., Gorton, M.P., Jackson, S.E., Neal, C.R., Chenery,
1008 S.P., 1997. A Compilation of New and Published Major and Trace Element Data for NIST
1009 SRM 610 and NIST SRM 612 Glass Reference Materials. Geostand. Geoanalytical Res. 21,
1010 115–144. https://doi.org/10.1111/j.1751-908X.1997.tb00538.x

1011 Pironon, J., 2020. Constraining fluid and diagenetic events in sedimentary basins by combining
1012 fluid inclusion data with burial models: discussion and recommendations, in: Lecumberri-
1013 Sanchez, P., Steele-MacInnis, M. (Eds.), Fluid And Melt Inclusions: Applications To Geologic
1014 Processes. Mineralogical Association of Canada, Ontario, pp. 1–14.

1015 Pollack, H.N., Cercone, K.R., 1994. Anomalous thermal maturities caused by carbonaceous
1016 sediments. Basin Res. 6, 47–51. https://doi.org/10.1111/j.1365-2117.1994.tb00074.x

1017 Renard, S., Pironon, J., Sterpenich, J., Carpentier, C., Lescanne, M., Gaucher, E.C., 2019.
1018 Diagenesis in Mesozoic carbonate rocks in the North Pyrénées (France) from mineralogy and
1019 fluid inclusion analysis: Example of Rousse reservoir and caprock. Chem. Geol. 508, 30–46.
1020 https://doi.org/10.1016/j.chemgeo.2018.06.017

1021 Roedder, E., 1990. Fluid inclusion analysis—Prologue and epilogue. Geochim. Cosmochim. Acta
1022 54, 495–507. https://doi.org/10.1016/0016-7037(90)90347-N

1023 Salardon, R., Carpentier, C., Bellahsen, N., Pironon, J., France-Lanord, C., 2017. Interactions
1024 between tectonics and fluid circulations in an inverted hyper-extended basin: Example of
1025 mesozoic carbonate rocks of the western North Pyrenean Zone (Chaînons Béarnais, France).
1026 Mar. Pet. Geol. 80, 563–586. https://doi.org/10.1016/j.marpetgeo.2016.11.018

1027 Scribano, V., Carbone, S., Manuella, F.C., Hovland, M., Rueslåtten, H., Johnsen, H.-K., 2017.
1028 Origin of salt giants in abyssal serpentinite systems. Int. J. Earth Sci. 106, 2595–2608.
1029 https://doi.org/10.1007/s00531-017-1448-y

1030 Sejourné, C., 1995. Bassin d'Arzacq, Aquitaine. Simulation de la maturité des roches mères. Elf
1031 Aquitaine Prod. 94, 120.

1032 Teixell, A., Labaume, P., Lagabrielle, Y., 2016. The crustal evolution of the west-central Pyrenees

1033 revisited: Inferences from a new kinematic scenario. Comptes Rendus Geosci. 348, 257–267.
1034 https://doi.org/10.1016/j.crte.2015.10.010

1035 Thiéry, R., Pironon, J., Walgenwitz, F., Montel, F., 2002. Individual characterization of petroleum
1036 fluid inclusions (composition and P–T trapping conditions) by microthermometry and confocal
1037 laser scanning microscopy: inferences from applied thermodynamics of oils. Mar. Pet. Geol.
1038 19, 847–859. https://doi.org/10.1016/S0264-8172(02)00110-1

1039 Veizer, J., Ala, D., Azmy, K., Bruckschen, P., Buhl, D., Bruhn, F., Carden, G.A.F., Diener, A.,
1040 Ebneth, S., Godderis, Y., Jasper, T., Korte, C., Pawellek, F., Podlaha, O.G., Strauss, H.,
1041 1999. 87Sr/86Sr, δ13C and δ18O evolution of Phanerozoic seawater. Chem. Geol. 161, 59–
1042 88. https://doi.org/10.1016/S0009-2541(99)00081-9

1043 Wu, J., Liu, S., Wang, G., Zhao, Y., Sun, W., Song, J., Tian, Y., 2016. Multi-stage hydrocarbon
1044 accumulation and formation pressure evolution in Sinian Dengying Formation-Cambrian
1045 Longwangmiao Formation, Gaoshiti-Moxi structure, Sichuan Basin. J. Earth Sci.
1046 https://doi.org/10.1007/s12583-016-0706-4

1047 Zhang, Y.-G., Frantz, J.D., 1987. Determination of the homogenization temperatures and densities
1048 of supercritical fluids in the system NaClKClCaCl2H2O using synthetic fluid inclusions. Chem.
1049 Geol. 64, 335–350. https://doi.org/10.1016/0009-2541(87)90012-X

1050

1051